Trajectory Estimation for Particles Observed in the Vicinity of (101955) Bennu

JGR Planets

RESEARCH ARTICLE
10.1029/2019JE006363

Special Section:
Exploration of the Activity of Asteroid (101955) Bennu

Trajectory Estimation for Particles Observed in the Vicinity of (101955) Bennu

S. R. Chesley[1], A. S. French[2], A. B. Davis[2], R. A. Jacobson[1], M. Brozović[1], D. Farnocchia[1], S. Selznick[3], A. J. Liounis[4], C. W. Hergenrother[3], M. C. Moreau[4], J. Pelgrift[5], E. Lessac-Chenen[5], J. L. Molaro[6], R. S. Park[1], B. Rozitis[7], D. J. Scheeres[2], Y. Takahashi[1], D. Vokrouhlický[8], C. W. V. Wolner[3], C. Adam[5], B. J. Bos[4], E. J. Christensen[3], J. P. Emery[9], J. M. Leonard[5], J. W. McMahon[2], M. C. Nolan[3], F. C. Shelly[3], and D. S. Lauretta[3]

[1]Jet Propulsion Laboratory, California Institute of Technology, Pasadena, CA, USA, [2]Smead Department of Aerospace Engineering Sciences, University of Colorado Boulder, Boulder, CO, USA, [3]Lunar and Planetary Laboratory, University of Arizona, Tucson, AZ, USA, [4]Goddard Space Flight Center, Greenbelt, MD, USA, [5]KinetX Aerospace, Simi Valley, CA, USA, [6]Planetary Science Institute, Tucson, AZ, USA, [7]Planetary and Space Sciences, School of Physical Sciences, The Open University, Milton Keynes, UK, [8]Institute of Astronomy, Charles University, Prague, Czech Republic, [9]Department of Astronomy and Planetary Science, Northern Arizona University, Flagstaff, AZ, USA

This article is a companion to Hergenrother et al. (2020), https://doi.org/10.1029/2020JE006381.

Key Points:
- Most of the 313 particles we study have suborbital trajectories, but some orbit Bennu and others directly escape
- The particles appear to have flake-like shapes and have effective diameters 0.22–6.1 cm with median 0.74 cm
- Ejections tend to take place in the local afternoon and evening but can occur anytime

Correspondence to:
S. R. Chesley,
steve.chesley@jpl.nasa.gov

Citation:
Chesley, S. R., French, A. S., Davis, A. B., Jacobson, R. A., Brozović, M., Farnocchia, D., et al. (2020). Trajectory estimation for particles observed in the vicinity of (101955) Bennu. *Journal of Geophysical Research: Planets*, *125*, e2019JE006363. https://doi.org/10.1029/2019JE006363

Received 31 DEC 2019
Accepted 1 JUN 2020
Accepted article online 8 JUL 2020

Abstract We analyze the trajectories of 313 particles seen in the near-Bennu environment between December 2018 and September 2019. Of these, 65% follow suborbital trajectories, 20% undergo more than one orbital revolution around the asteroid, and 15% directly escape on hyperbolic trajectories. The median lifetime of these particles is ~6 hr. The trajectories are sensitive to Bennu's gravitational field, which allows us to reliably estimate the spherical harmonic coefficients through degree 8 and to resolve nonuniform mass distribution through degree 3. The particles are perturbed by solar radiation pressure, enabling effective area-to-mass ratios to be estimated. By assuming that particles are oblate ellipsoids of revolution, and incorporating photometric measurements, we find a median axis ratio of 0.27 and diameters for equivalent-volume spheres ranging from 0.22–6.1 cm, with median 0.74 cm. Our size distribution agrees well with that predicted for fragmentation due to diurnal thermal cycling. Detailed models of known accelerations do not produce a match to the observed trajectories, so we also estimate empirical accelerations. These accelerations appear to be related to mismodeling of radiation pressure, but we cannot rule out contributions from mass loss. Most ejections take place at local solar times in the afternoon and evening (12:00–24:00), although they occur at any time of day. We independently identify ten ejection events, some of which have previously been reported. We document a case where a particle ricocheted off the surface, revealing a coefficient of restitution 0.57±0.01 and demonstrating that some apparent ejections are not related to surface processes.

Plain Language Summary The Origins, Spectral Interpretation, Resource Identification, Security, Regolith Explorer (OSIRIS-REx) mission discovered that near-Earth asteroid (101955) Bennu is periodically ejecting small particles from its surface, placing it in the uncommon class of "active asteroids." We linked together individual detections of ejected particles and used numerical models of the forces acting on them to ascertain their trajectories and fates. We found that most particles have suborbital trajectories, meaning they fall back to Bennu's surface shortly after being ejected, but some orbit Bennu for days at a time, and some escape directly into space. From the particle trajectories, we are able to estimate their sizes (comparable to pebbles, from a few millimeters to a few centimeters in diameter) and shapes (probably flake like). Their trajectories also make it possible to estimate Bennu's gravity field more precisely than spacecraft measurements and help shed light on the possible causes of the ejections.

1. Introduction

One of the early surprises for the National Aeronautics and Space Administration (NASA)'s Origins, Spectral Interpretation, Resource Identification, Security, Regolith Explorer (OSIRIS-REx) asteroid sample return mission occurred shortly after the spacecraft entered into orbit around its target, the near-Earth asteroid (101955) Bennu. OSIRIS-REx navigational images from 6 January 2019 revealed that particles

were being ejected from the asteroid surface into the spacecraft environs (Hergenrother et al., 2019). The particles were small, initially estimated to be roughly 1–10 cm in diameter, and the velocities were relatively low, up to a few meters per second; thus, the immediate concerns about spacecraft safety were quickly allayed (Lauretta et al., 2019). However, these particle detections raised questions. For example, what is causing the particle ejections? What are the physical properties of the particles, such as mass, size, shape, and albedo? What are the ejection circumstances, such as velocity and time of day? What is the frequency of ejection events? Our paper builds on the work of Lauretta et al. (2019) by computing the trajectories of hundreds of ejected particles detected between December 2018 and September 2019. This longer time frame and greater number of analyzed particles allows us to make further inferences and draw conclusions about the particle dynamics in Bennu's environment and, in turn, to add constraints to the nature of the ejection mechanism.

The discovery of small particles leaving its surface puts Bennu in the category of active asteroids. Until recent decades, comets were distinguished from asteroids primarily by the presence of observable activity, with asteroids being generally presumed as inert bodies. The discovery of the so-called main-belt comets represented a fundamental shift in the way asteroids are conceived. We now have many asteroids—in both the main belt and near-Earth populations—that appear to be active, and there are several disparate mechanisms that appear to be causing the activity. Sublimation of volatiles appears as a likely explanation for many (Hsieh & Jewitt, 2006), while ejecta from small impactors has been proposed for others, and these two phenomena could work hand in hand, with small impactors exposing buried ices, leading to sustained activity after the impact ejecta have dispersed (Jewitt et al., 2015). Other cases appear to be driven by rotational fission, with rapid rotators episodically shedding material (Jewitt et al., 2013). The possibility that thermal cycling could lead to sudden fracturing and energetic release of fragments has been studied in the laboratory (Delbo et al., 2014) and has been proposed for the activity seen from (3200) Phaethon at small heliocentric distance (Li & Jewitt, 2013) and to explain the apparent paucity of small, dark asteroids at low perihelion distances (Granvik et al., 2016).

In the context of Bennu's activity, multiple mechanisms have recently been studied. From high-resolution thermal modeling, Rozitis et al. (2020) conclude that ice sublimation is not a plausible explanation but that high diurnal temperature amplitudes create conditions favorable to thermal fracturing. Molaro et al. (2020) test thermal fracturing models, finding that thermal fracturing should lead to exfoliation on Bennu and could eject centimeter-scale particles at speeds up to meters per second, consistent with Bennu's observed activity (Lauretta et al., 2019). Bottke et al. (2020) examine the hypervelocity meteoroid flux at Bennu and report that such impacts could readily explain the evident energy and frequency of particle ejection events, predicting—like Molaro et al. (2020)—that most such ejections should occur in the afternoon and evening, local solar time (LST) on Bennu. Both the meteoroid and thermal fracturing models predict increased activity at lower heliocentric distances, that is, at perihelion.

We present a catalog of particle trajectories that is based on dedicated and serendipitous tracking of their positions and that is affected by significant selection effects. While Bennu's Hill sphere extends to 31 km (Rieger et al., 2019), our detections are from a nearby spacecraft with its camera oriented toward Bennu; thus, our particles occupy only a small fraction of the Hill sphere. Also, we require at least three detections to obtain an orbital solution, which eliminates the possibility of obtaining orbits of objects that rapidly leave Bennu's vicinity or are only lofted for a brief period. Finally, there is a lower size limit beyond which the particles are too small to allow sufficient signal in the images. Taken together, these limitations imply that we have only those particles that are large enough and remain in flight and near Bennu for long enough to estimate the trajectory. Another important consideration is that, over the 9 months for which we have data, the cadence of particle tracking images varied greatly, which has a profound effect on our ability to link detections to discern particle trajectories. The exact nature and effect of these selection effects remains as work to be done, but with the trajectories presented here, we can already see a portrait of the rich dynamical environment that these particles inhabit.

The dynamics of particles in orbit about a small body and strongly perturbed by solar radiation pressure (SRP) has been studied over the past decades for both cometary and asteroidal bodies. For comets, the impetus is to study the dynamics of lofted particles that are large enough to remain bound to the nucleus. To do this, Richter and Keller (1995) developed an analysis looking at the dynamics of the particles using

angular momentum and the eccentricity vectors as independent variables. Independently, Mignard and Henon (1984) showed that this basic problem was integrable when averaged and worked out the details of that solution for a body in a circular orbit about the Sun. In a later series of papers, Scheeres and coworkers combined and generalized these studies, showing that the integrable solution extends to the case when the small body is in an elliptic orbit about the Sun and can be generalized to a noncannonball model (Rosengren & Scheeres, 2014; Scheeres, 1999, 2012a). Contemporaneous with these studies was work by Dankowicz (1994, 1995), and later Scheeres and Marzari (2002), that developed conditions for particle capture when subject to SRP. When combined, these models provide an accurate representation of motion about a small body when strongly perturbed by SRP. A main application of these studies is to spacecraft dynamics about asteroids and comets (Scheeres, 2012b), and the OSIRIS-REx mission uses this theory for the design of its stable terminator orbits.

The hallmarks of motion of a particle in orbit about a small body and perturbed by SRP can be fully understood by combining these analyses. When bound, the motion in terms of orbit elements will be periodic, with a period less than one asteroid year, and with the period decreasing with increasing SRP perturbation strength. Thus, a particle ejected from the surface of an asteroid will tend to come back to the surface again, after a period of time, as the initial ejection orbit elements will repeat. Still, the time between ejection and this return can be on the order of days to weeks and months, depending on the SRP strength and ejection conditions. For particles that move far from the small body, yet are still bound, their motion can closely mimic the ideal SRP solutions. For particles ejected at lower speeds and which remain closer to the asteroid, the effect of the asteroid oblateness and higher-order gravity field coefficients can have as large an effect as the SRP perturbations and create motion that is more chaotic in general (Scheeres, 2012a). However, as we show in section 5.6, such interactions also create an opportunity as they can provide insight into the mass distribution of the asteroid.

Our work dovetails with that of McMahon et al. (2020), who generated a large number of synthetic trajectories in the Bennu environment, systematically covering the range of particle ejection locations and circumstances. Their work provides a useful touchstone for the broad range of possible particle dynamics near Bennu, while our work documents what is actually seen. Taken together these approaches represent a pathway to eventual debiasing of the observed particle population.

In the following sections, we describe our observational data (section 2) and then provide the details of our dynamical model (section 3) and the orbit fitting process (section 4). This is followed by a description and discussion of the various results (section 5). We close with a listing of key conclusions.

2. Observational Data

The observational data for this effort are from a catalog of transient detections seen in images taken by the OSIRIS-REx NavCam 1 imager, part of the Touch and Go Camera System (TAGCAMS) (Bos et al., 2018), from December 2018 through October 2019. These image data were reduced to right ascension (RA) and declination (DEC) measurements as seen from the camera at the midexposure time. Details of the image reduction process are presented by Liounis et al. (2020), and here we provide only a summary.

The NavCam 1 images used for particle tracking were long-exposure images (typically ~5 s) that were intentionally designed to reveal background stars, leaving Bennu heavily overexposed as a consequence. Initially, these images were part of optical navigation image sequences, where the presence of stars allowed an accurate estimate of the camera orientation for contemporaneous short-exposure images that revealed navigational landmarks on the surface of the asteroid. In later stages of the mission, image sequences dedicated to particle monitoring used only the long-exposure images.

A temperature-dependent focal plane distortion model was used for the NavCam 1 images (Liounis et al., 2020), while the image pointing solution was obtained by matching cataloged reference stars to image sources. Image sources that reasonably matched a Gaussian point spread function and were not matched to a star were presumed to be candidate particle detections.

The active focal plane for NavCam 1 is 2,592×1,944 pixels, leading to a field of view of 44° × 32°, given the 288 μrad pixel scale (~1 arcmin) and accounting for optical distortion (Bos et al., 2018). At typical spacecraft-

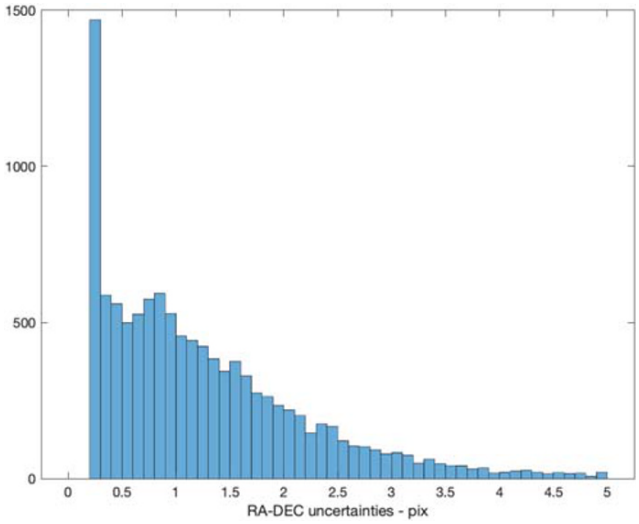

Figure 1. Distribution of RA and DEC uncertainties for the detections used in the trajectory fits.

particle distances of ~1 km, this pixel scale translates to about 30 cm per pixel. Thus, given that the particle sizes are a few centimeters at most, the particles were not resolved in images. The point spread function for particle detections typically has a full-width, half-max of ~1.7 pixels (Hergenrother et al., 2020).

The image-processing approach (Liounis et al., 2020) that we developed to mine the images for candidate particle detections was deliberately designed to ensure a high completeness, with the cost being a high rate of spurious detections. From 1 December 2018 through 14 October 2019, the system identified ~18 million candidate detections from 12,640 images, for an average of 1,400 detections per image. These potential detections include a large fraction of spurious detections that can arise from a variety of causes, including cosmic rays, the high background levels near Bennu's illuminated limb, unlinked stars, and camera artifacts such as stray light and hot pixels. Based on visual inspection of images, we believe that only a few percent of such detections are not spurious.

The image-processing pipeline assigns an integer quality code $1 \leq Q \leq 5$ based on a variety of parameters including signal-to-noise ratio (SNR) and goodness of fit to a two-dimensional Gaussian point spread function (Liounis et al., 2020). Here Q=1 indicates a probably spurious detection (or a detection matched to a catalog star). Q=2 indicates a low-confidence detection that in many cases is associated with a hot pixel or an unmatched star. Increasing values of Q denote increasing levels of confidence that the detection is associated with a particle.

The pipeline also assigns an astrometric error estimate to candidate detections, which is based heavily on the detection SNR (Liounis et al., 2020). NavCam 1 significantly undersamples the point spread function (Bos et al., 2020), and so the pipeline astrometric uncertainties are greater than would be expected for a well sampled detection. For our trajectory fits, we take a conservative approach, doubling the pipeline uncertainty and applying a floor uncertainty of 0.25 pixels. Figure 1 shows the distribution of astrometric uncertainty used in the fits. The 0.25 pixel floor is clearly apparent in the plot, which cuts off at 5 pixels on the right. Less than 3% of detections have uncertainty over 5 pixels. The median uncertainty is 1.05 pixels.

The process of linking detections of a single object to produce a data set for orbit estimation makes use of the intermediate linking step of the *track*. A track is a set of detections close together in time, covering up to a few hours duration, that are linked together by virtue of their compatible plane of sky motion. The track is generally composed of detections that reflect approximately uniform rectilinear motion on the sky. The tracks that we used for orbit estimation were largely derived from visual inspection and blinking of images, or through software tools. See Liounis et al. (2020) and Hergenrother et al. (2020) for details. If there are at least three detections in a track, it may be suitable for orbit fitting. The next level in the linking process is linking tracks of the same object, which we describe in section 4.3.

The volume of detections is shown in Figure 2, which shows clearly that only a tiny fraction of candidate detections have been included in orbital fits. This is in part due to the deliberately high rate of false detections, but the imaging cadence is also a decisive factor. For example, the large number of detections in Orbital B (July 2019) was acquired at a cadence and asteroid range that was unfavorable for linking more than two detections into tracks (Hergenrother et al., 2020), leaving many unlinked pairs of detections. While these data may eventually be linked, it will require more sophisticated algorithms (see, e.g., Denneau et al., 2013) than we have implemented so far.

Lauretta et al. (2019) discuss the possibility that the OSIRIS-REx Laser Altimeter (OLA; Daly et al., 2017) may have detected particles in Bennu's environment. We have compared the off-Bennu returns reported by OLA with our particle trajectories but have not found a match. This only indicates that none of our particles are among the ones possibly detected by OLA and does not imply that the reported off-Bennu OLA detections were not associated with particles.

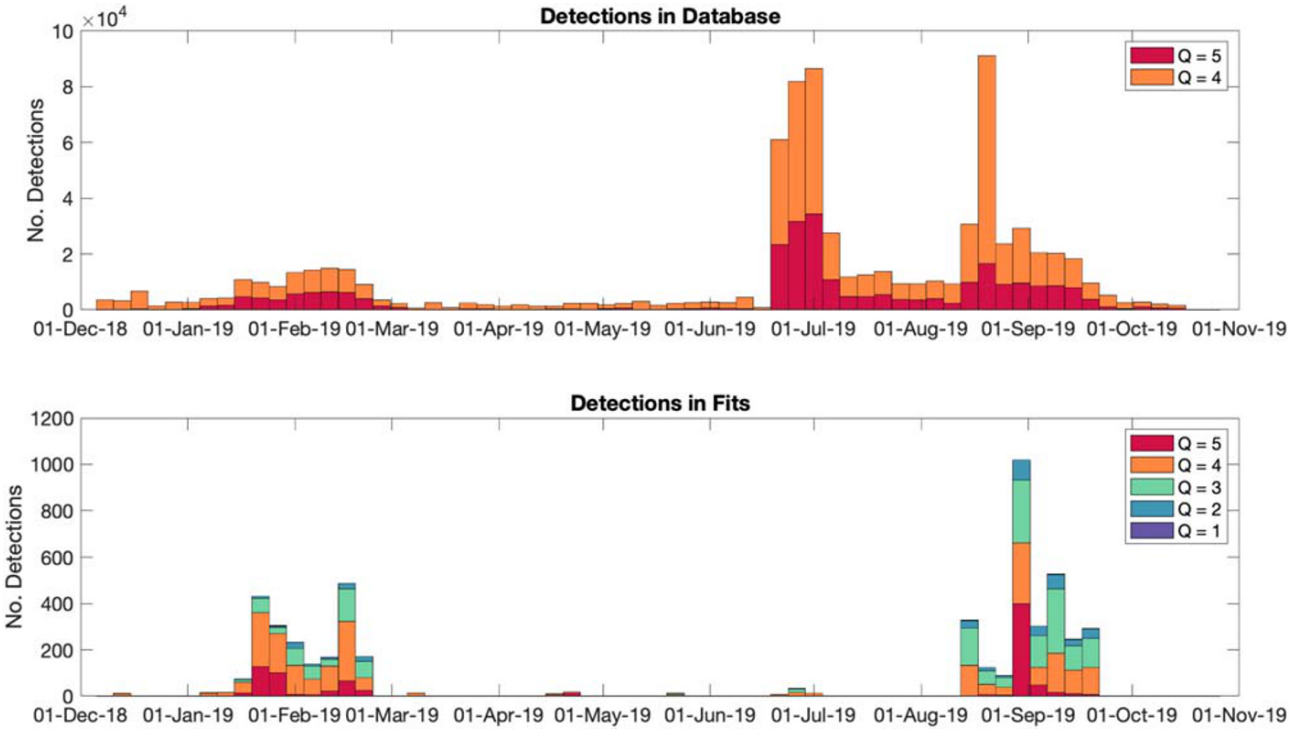

Figure 2. Times of detections present in pipeline database (upper panel) and used in orbital fits (lower panel). Q is a quality code, as described in the text, with larger values indicating higher confidence. In the upper panel we show only detections with $Q \geq 4$ to improve clarity. Most orbit estimates were obtained from detections in the OSIRIS-REx Orbital A (January–February 2019) and Orbital C (August–September 2019) mission phases, when the spacecraft was orbiting at a radius of ~1.5 km.

3. Force Models

Modeling the trajectory of a small particle moving in the Bennu environment requires a detailed model of the forces acting on the particle. Table 1 lists the different forces known to be acting on the particles. In addition to gravity, the effect of radiation pressure on the particles is significant. Direct SRP is particularly so, but more subtle effects such as radiation from Bennu and shadowing by Bennu cannot be ignored.

In the early stages of this effort, it proved difficult to fit the observational data, so we worked to improve the force model fidelity as much as possible. And yet, there were still clear signatures for unmodeled forces, which we were able to estimate. In the following subsections, we discuss the fundamental components of our force model, as well as some small forces that may be acting but are not explicitly modeled. Detailed results related to these models are discussed in section 5.

Table 1
Elements of the Particle Force Model, Including an Approximate Magnitude for a Particle of Area-to-Mass Ratio η=0.075 m^2/kg at an Orbital Radius of 500 m and Above the Subsolar Point on Bennu When Near Perihelion

Source of acceleration	Acceleration (km/s^2)
Bennu point mass	3×10^{-8}
Bennu gravitational harmonics	6×10^{-10}
Direct solar radiation	4×10^{-10}
Infrared emission from Bennu	5×10^{-11}
Sunlight reflected from Bennu	2×10^{-11}
Unmodeled forces	$<1\times10^{-11}$
Reflected pressure: Direct solar	3×10^{-12}
Reflected pressure: Infrared from Bennu	3×10^{-13}
Reflected pressure: Sunlight from Bennu	1×10^{-13}
Thermal emission from particle[a]	$\lesssim 8\times10^{-13}$
Solar tide	5×10^{-14}
Poynting-Robertson Effect[a]	4×10^{-14}

[a]Not explicitly included in our force model.

3.1. Gravity

We modeled the gravitational acceleration for a particle in Bennu's environment through the classical spherical harmonic expansion with normalized coefficients C_{nm} and S_{nm}, where n and m are, respectively, the degree and order of the expansion (e.g., McMahon et al., 2018). We also use the common notation for zonal terms in the expansion: $J_n = -C_{n0}$. Consistent with the circumscribing sphere of the Bennu shape model (Barnouin et al., 2019), we used 290 m as the reference radius in the expansion. The sensitivity of the particle trajectory allowed us to estimate not only the gravitational parameter GM of Bennu but also many of the harmonic coefficients.

Our initial gravitational force model was based on the OSIRIS-REx shape model (Barnouin et al., 2019), assuming uniform density (Werner, 1997).

From this shape, we derived the associated spherical harmonic coefficients and, as detailed in section 4.2, we apply soft constraints to prevent the estimate from wandering farther from these values than is required by the data.

Many of the particles spend a small fraction of their orbit beneath Bennu's Brillouin (circumscribing) sphere. We know that the standard spherical harmonic expansion does not converge globally beneath this sphere; however, the behavior of this divergence is difficult to predict analytically and in general does not occur immediately at the Brillouin boundary (Jekeli, 1983; Reimond & Baur, 2016). Thus, we performed numerical tests that compared the spherical harmonic model to the constant density polyhedron model (Werner & Scheeres, 1996) to quantify this behavior. For the particular case of particles orbiting about Bennu, we found that the effect due to divergence is small when compared to truncation error at least up to degree 16, well beyond what can be inferred from the particle detection data. This can likely be attributed to Bennu's roughly spherical shape. In the strictest sense it is the *infinite* series that is divergent, and we note that the truncated series is smooth and continuous everywhere except at the expansion's origin (Bennu's center of mass), which means that even if the truncated expansion does not perfectly capture the dynamics, the partial deriviatives needed for orbit determination and mapping are still valid.

3.2. Radiation Pressure

3.2.1. SRP

The acceleration due to solar radiation impinging on a particle can be written as

$$\mathbf{a}_{\mathrm{SRP}} = \Psi\eta\frac{\mathbf{r}_\odot}{r_\odot^3},$$

where $\mathbf{r}_\odot$ is the vector from the Sun to the particle and η is the ratio of cross-sectional area to mass for the particle. Radiation pressure from photons reflected or scattered by the particle is discussed below. For this work, we take a solar irradiance of 1,367 W/m^2 (Fröhlich & London, 1986), leading to a SRP constant $\Psi = 1.016{\times}10^{17}$ N and associated SRP of 4.56 μPa at 1 au.

If we consider a notional spherical particle of 1 cm in diameter and a bulk density of 2 g/cm^3, then we have $\eta = 0.075$ m^2/kg. Given the orbit of Bennu, SRP on our notional particle causes an acceleration ranging from a peak of $4.2{\times}10^{-10}$ km/s^2 at perihelion (0.90 au) down to $1.8{\times}10^{-10}$ km/s^2 at aphelion (1.36 au). As we shall see below, the trajectories of many particles are strongly sensitive to this acceleration.

Many particles enter Bennu's shadow, during which time SRP is not acting. We implement a high-fidelity shadowing model based on the detailed shape of Bennu. When the Sun is fully eclipsed by Bennu, as seen by the particle, SRP is neglected. When the Sun is partially eclipsed by Bennu, the fraction of the solar disk visible from the particle serves as a scale factor on SRP. We do not shift the direction of SRP during partial eclipse to account for the slightly offset centroid of the visible Sun.

Our model assumes a constant value of η, which we consider to be a reasonable approach given that the particles must be rapidly tumbling for any realistic partition between translational and rotational kinetic energy. Thus, while the instantaneous value of η may be evolving rapidly on short time scales (~1 s), a useful mean can be obtained with relatively short averaging intervals, far less than the time span of our observational data (hours to days).

3.2.2. Bennu Radiation Pressure

In addition to radiation arriving directly from the Sun, other solar radiation reaches the particles indirectly, most notably from the surface of Bennu. This comes in two forms, namely, reflected solar radiation and thermal emissions due to solar heating of the Bennu surface.

For solar radiation reflected from Bennu to the particle, often referred to as the *albedo effect*, we do a facet-wise summation of the reflected radiation for all Bennu facets that are visible to both the particle and the Sun. For a uniform geometric albedo $\mathscr{A}$ and Lambertian scattering, this can be written as (Borderies & Longaretti, 1990)

$$\mathbf{a}_{\mathrm{albedo}} = \frac{\mathscr{A}\Psi\eta}{\pi r_\odot^2}\sum_{i\in\mathscr{F}} A_i \cos\gamma_i \cos\alpha_i \frac{\mathbf{r}_i}{r_i^3},$$

where the area of the ith facet is denoted by A_i. Here γ_i is the emission angle from the center of the ith

facet to the particle, that is, the angle between the facet unit normal vector $\hat{\mathbf{n}}_i$ and the vector $\mathbf{r}_i$ from the facet center to the particle. Thus, $\cos\gamma_i = \hat{\mathbf{n}}_i \cdot \mathbf{r}_i / r_i$. Similarly, α_i is the solar incidence angle at the ith facet, so $\cos\alpha_i = -\hat{\mathbf{n}}_i \cdot \mathbf{r}_\odot / r_\odot$. The facets to be included in the summation are denoted by $\mathcal{F}$, which is the set of facet indices for which both $\cos\gamma_i$ and $\cos\alpha_i$ are positive.

For the infrared radiation pressure (IRP) from Bennu, surface temperatures were generated by the Advanced Thermophysical Model (ATPM) of Rozitis and Green (2011-2013) using the thermophysical properties of Bennu derived by Dellagiustina et al. (2019). The ATPM returns an interpolated temperature T_i at the ith facet from a look-up table of temperatures for each facet as a function of the LST in 1° steps. The effect of varying heliocentric distance $r_\odot$ from the reference value of the interpolation table $r_{\odot_{\mathrm{REF}}}$ was captured by scaling the reference temperature T_{REF} according to $(T/T_{\mathrm{REF}})^4 = (r_{\odot_{\mathrm{REF}}}/r_\odot)^2$. Now, with the temperature at each facet from the look-up table, we can compute the IRP acceleration as a sum over all facets visible to the particle:

$$\mathbf{a}_{\mathrm{IRP}} = \frac{\sigma\epsilon\eta}{c\pi} \sum_{i\in\mathcal{F}} T_i^4 A_i \cos\gamma_i \frac{\mathbf{r}_i}{r_i^3},$$

where σ is the Stefan-Boltzmann constant, ϵ is the Bennu emissivity (assumed to be 0.9 everywhere), and c is the speed of light. Here $\mathcal{F}$ is the set of facet indices for which $\cos\gamma_i > 0$.

This IRP model breaks down when the particle altitude is comparable to or below the shape model facet scale. We work past this problem by applying the force obtained at an altitude of 10 m whenever the particle falls below 10-m altitude. Altitudes below 10 m are rare and brief events, typically seen only in the few tens of seconds after ejection or before impact, and we do not consider this to be a significant source of force modeling error.

For both of these sources of radiation, albedo and IRP, we use the same polyhedral shape model mentioned above (Barnouin et al., 2019) to compute the associated acceleration. For our fits, we used a shape version with 3,072 facets (mean facet edge ~25 m), though we did test a variant with 4 times more facets (12,288 facets, mean edge length ~12.6 m) and found that the results did not depend upon which of the two models was used.

3.2.3. Reflected Radiation Pressure

The photons that impinge on a particle are responsible for direct radiation pressure, as discussed above for SRP, IRP, and the albedo effect. But some fraction of the photons that strike the particle are reflected or scattered away, leading to additional momentum transfer, which we refer to as *reflected radiation pressure*. Photons not reflected are absorbed, thus heating the particle, leading to subsequent emission of thermal photons. Here we discuss the momentum transfer due to reflected photons, and in section 3.2.4, we will discuss the possibility of accelerations due to thermal emission from the particle.

We do not have detailed models for the particle shapes, albedos, or light-scattering properties, so we adopt a simple model assuming spherical particles with Lambertian scattering. Under these assumptions, the ratio of reflected to direct radiation pressure is $\frac{4}{9}\mathscr{A}_{\mathrm{Bond}}$, where $\mathscr{A}_{\mathrm{Bond}}$ is the Bond albedo (Borderies & Longaretti, 1990). Thus, the total radiation pressure from a given source is

$$\mathbf{a}_{\mathrm{TOTAL}} = \left(1 + \frac{4}{9}\mathscr{A}_{\mathrm{Bond}}\right) \mathbf{a}_{\mathrm{DIRECT}}.$$

Here $\mathbf{a}_{\mathrm{DIRECT}}$ can alternately refer to $\mathbf{a}_{\mathrm{SRP}}$, $\mathbf{a}_{\mathrm{IRP}}$, or $\mathbf{a}_{\mathrm{albedo}}$, depending on the radiation source under consideration. We further assume $\mathscr{A}_{\mathrm{Bond}} = 0.016$ (Dellagiustina et al., 2019) so that reflected radiation pressure is 0.7% of the direct radiation pressure. As part of our orbit determination approach (discussed in section 4.2), we estimate the total radiation pressure by estimating the value of the term $\eta' = (1 + \frac{4}{9}\mathscr{A}_{\mathrm{Bond}})\eta$. Thus, when deriving area-to-mass ratios of the particles, we scale the estimated parameter to obtain $\eta = \eta'/1.007$.

We emphasize that there are several crucial and untested assumptions that go into our assessment of reflected radiation pressure. As mentioned above, we can reasonably suppose that the particles are rapidly tumbling, and thus, shape effects could be effectively modeled by a mean η, but the scattering properties and albedo are unknown. This could introduce a bias in our estimates of η but should still allow the orbit

estimation approach to obtain the correct η' and total acceleration $\mathbf{a}_{\mathrm{TOTAL}}$, which is important for the overall trajectory estimate.

3.2.4. Particle Thermal Emissions

It is well known that the Yarkovsky effect, a subtle acceleration due to the reaction force from thermal emission, can significantly alter an asteroid's heliocentric orbit over long time scales (see, e.g., Bottke et al., 2006; Vokrouhlický et al., 2015). Here we consider the possibility that thermal emission from particles may also affect their trajectories in an appreciable way.

The Yarkovsky effect depends nonlinearly on the rotation rate of the body in question, and yet our data provide no direct constraint on the particle rotation periods (Hergenrother et al., 2020). We do presume, however, that the partition between translational and rotational kinetic energy is not extreme. For a typical 1-cm particle with ejection velocity of the order of 20 cm/s, the rotation period must be less than 1 s, assuming that at least 1% of the particle kinetic energy is due to rotation. Taking an equipartition between translational and rotational kinetic energies yields a rotation period of 0.1 s, corresponding to the shortest periods considered here.

Such high spin rates raise the question of whether particles should be expected to have the strength to avoid rotational bursting. Sánchez and Scheeres (2014) provide an expression for the failure spin rate of an idealized body held together by self-gravity and cohesion. This allows them to bound the cohesive strength σ of a rapidly spinning particle according to

$$\sigma > \frac{\rho d^2}{4}\left[\omega^2 - \frac{4\pi G\rho}{3}\right],$$

where ω is the rotation rate, ρ is the density of the particle, d is its diameter and G is the gravitational constant. For our presumed spin rates and reasonable meteorite bulk densities, the gravitational term, $4\pi G\rho/3$, is orders of magnitude less than the rotational term, ω^2, and can be neglected. Thus, the strength limit can be simplified to $\sigma > \rho d^2\omega^2/4$. Then, assuming a particle of diameter 1 cm and density of 2,000 kg/m^3 spinning at periods from 0.1–1 s, the minimum particle strength must be in the range 2–200 Pa, far below the cohesive strengths of meteorites which, at smallest, are at the several kPa level (Scheeres et al., 2015). Thus, the particle need not have much strength to hold together.

Returning to the Yarkovsky modeling, we used a simple approach based on linearized heat conduction theory. Assuming spherical and homogeneous particles, Vokrouhlický (1998) estimated thermal accelerations based on rotational cycling (diurnal effect; in this crude estimate, we neglect the seasonal effect). For quantitative conclusions, we adopted a thermal inertia of 350 J m^{-2} K^{-1} s$^{-\frac{1}{2}}$, roughly corresponding to the pebble component of Bennu's surface, and a thermal conductivity of 0.1 W m^{-1} K^{-1}. To maximize the role of the diurnal thermal component, we assumed the instantaneous location of the Sun at the particle's equator (in the plane perpendicular to the instantaneous rotation axis). We tested particle sizes between 1 and 10 cm and assumed their rotation period ranged between 0.1 and 10 s.

With these parameters set, the penetration depth of the diurnal thermal wave ranges between about a millimeter (for the shortest periods) to a little less than a centimeter (for the longest periods; top panel on Figure 3). The particles are thus barely in the large-body regime, with the exception of the slowly rotating centimeter-sized particles, which are already in the small-body regime (thus efficiently conducting heat throughout their volume). In the high-inertia situation considered here, the diurnal thermal parameter ranges between several tens (for the longest periods) to several hundreds (for the shortest periods), implying rather efficient longitudinal equalizing of temperature (see, e.g., Bottke et al., 2006; Vokrouhlický et al., 2015). This is the principal reason for making the total thermal acceleration very small for the short rotation periods.

Figure 3, bottom panel, shows the total thermal acceleration expressed as a fraction of the direct SRP for various particle sizes and as a function of the rotation period. Given that particle spin periods should be <1 s, the fraction is only $\lesssim 2\times10^{-3}$, quite small compared to other forces at play. For all combinations in our parameter space, this fraction ranges between $\simeq$0.001 and $\simeq$0.01. Even extending the rotation periods by an order of magnitude larger, the computed fraction of the thermal acceleration stalls at a few percent of SRP. This is

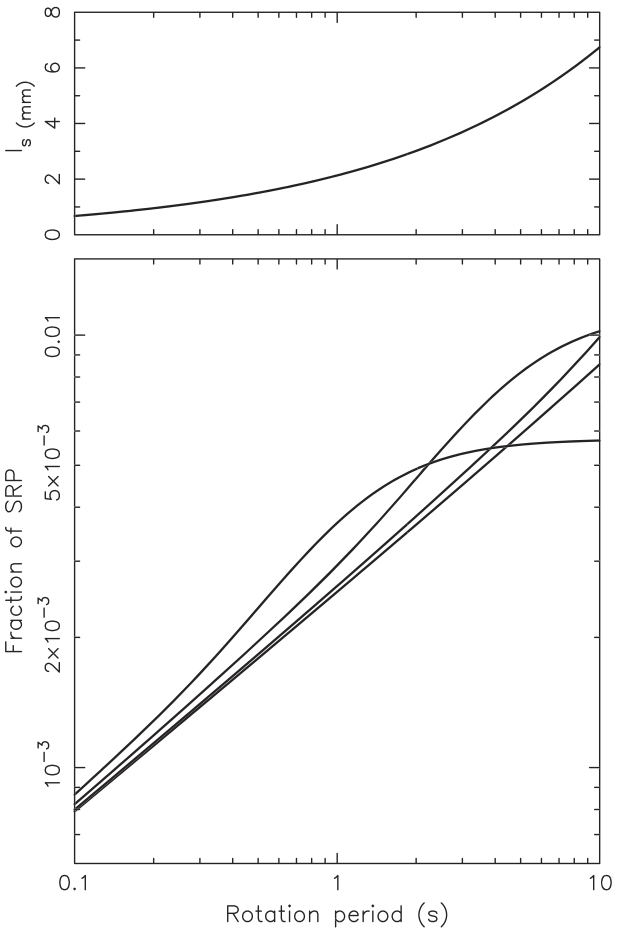

Figure 3. Top panel: Skin depth ℓ_s for the diurnal thermal wave as a function of rotation period. Bottom panel: Thermal recoil acceleration as a fraction of direct SRP versus rotation period. The lower plot assumes spherical particles of diameters 1, 2, 5, and 10 cm (from upper to lower curve at left of plot).

because in that case the thermal penetration depth becomes comparable to, or larger than, the particle sizes, and the heat conduction across the particles equalize the surface temperature.

The takeaway message is that thermal recoil acceleration on particles is ~3 orders of magnitude less than SRP, and roughly an order of magnitude less than reflected solar radiation. We neglect this as a source of acceleration in our dynamical model.

3.3. Other Known Accelerations

The third-body gravitational perturbation from the Sun can be cast as the differential acceleration between a particle near Bennu and Bennu itself, also known as solar tide. For a particle ~0.25 km above the subsolar point on Bennu when at perihelion, this acceleration is roughly 5×10^{-14} km/s^2. We include this term in our force model, despite the fact that it is not a significant perturbation for the particles.

Poynting-Robertson acceleration is a very slight acceleration related to SRP. Stellar aberration related to the velocity v of the observer moves the apparent place of the Sun by an angle of order v/c, for an observer on a circular orbit. This leads to a transverse acceleration $\sim10^{-4}$ of SRP, or $\sim4\times10^{-14}$ km/s^2 for a particle near Bennu at perihelion. Our force model neglects this perturbation.

3.4. Empirical Accelerations

As we discuss in more detail below, the elements of the force model discussed so far did not lead to reasonable postfit residuals of the astrometric data. Given this inability to match the observations to an integrated trajectory, it became clear that either mismodeling of the observations was responsible or there were unmodeled forces at play. After carefully verifying the observation model, and accounting for observation model uncertainties, we concluded that additional accelerations of order 10^{-12} km/s^2 to as much as 10^{-11} km/s^2 were acting on the particles. In a later section we discuss in greater detail the orbit determination approach, but here we describe our model for empirical accelerations.

The empirical acceleration model assigns an acceleration vector $\mathbf{a}_i = \mathbf{a}(t_i)$ at a series of times t_i spanning the observation interval. The times t_i are arbitrary, but in practice, we select a constant time interval Δt so that $t_{i+1} = t_i + \Delta t$. The acceleration at times between the t_i nodes are obtained through linear interpolation, according to

$$\mathbf{a}(t) = \mathbf{a}_i + \frac{\mathbf{a}_{i+1} - \mathbf{a}_i}{\Delta t}(t - t_i) \quad \text{for} \quad t \in [t_i,\, t_{i+1}].$$

Because the empirical acceleration model is continuous in time, it does not pose difficulty for our particle integrator, which requires an integrator restart at all discontinuities.

The components of each $\mathbf{a}_i$ are estimable parameters, with a priori constraints. Estimating these empirical acceleration parameters serves to ensure that the modeled trajectory of the particle allows it to reach the location where it was observed to be and thus allows fits consistent with the observational uncertainty. In cases where there are extended time gaps in observation coverage, the $\mathbf{a}_i$ implement what can be considered the minimum thrust transfer from the time of the earlier observation to the time of the later observations.

4. Orbit Estimation Approach

4.1. Initial Orbit Determination

Linked sets of observations (single tracks) with at least three detections are fed into a three-stage orbit determination process. The first stage is the initial orbit determination (IOD). Initially, nothing is known about a

particle's orbit, other than that it produced the observations (assuming the associations are correct). The role of IOD is to generate one or more candidate trajectories that could have produced the observations. There are many classes of IOD algorithms that have been designed for various orbital problems. Here, we use a general-purpose IOD algorithm that performs a grid search/simplex optimization over a range of orbital elements to minimize the RMS (root mean square) of the observation residuals. This method is robust in the sense that it explores a wide range of possible orbits and in the sense that it is not limited by any observability constraints (i.e., it is insensitive to observing geometry). It is also relatively quick to converge because it only deals with Keplerian dynamics. However, in some cases, particularly when there are few (e.g., three to five) detections, the algorithm will converge to an erroneous local minimum that may be far from the true solution. Typically, this can only be determined to be the case with the addition of more observations, or through the use of some external criteria (i.e., dynamical arguments, visual inspection, etc.). Tracks that could not be fit with residual RMS <8 pixels were rejected from consideration.

4.2. Orbit Determination

Next, the resultant IOD solution is fed into a more conventional orbit determination (OD) software suite derived from Jet Propulsion Laboratory (JPL)'s Orbit Determination Program (MIRAGE/ODP) that is better tuned for satellite ephemeris estimation. This step performs iterative differential corrections to the trajectory to minimize the sum of the squares of the observation residuals. In particular, it implements a batched sequential weighted square root information filter (SRIF) that supports stochastic parameter estimation (white noise or exponentially correlated). This and similar algorithms are well documented in the literature (e.g., Bierman, 1977; Moyer, 2003; Tapley et al., 2004) and have been at the heart of orbit determination for the past several decades. It is at this stage where higher-fidelity force modeling is added and a priori uncertainties are applied.

In a system that is well constrained by the observational data, the a priori uncertainty can be set to infinity (i.e., zero a priori information) and the filter will converge, provided the initial IOD estimate is within the linear regime of the correct solution. However, when fitting a single track (with few detections) to an orbit, the system can be poorly constrained by the observations, often because there are one or more linear combinations of the components of the state vector that are unobservable. In practice, this typically results in filter divergence, which can be mitigated by constraining the estimated parameters to the IOD solution through the use of suitable a priori covariance matrix, which enforces the hypothesis that the IOD solution is approximately correct. Here, we set the a priori constraints based on the scale of the Bennu system. Each component of the particle's position is assigned a 250 m a priori uncertainty, which in three dimensions roughly equates to Bennu's volume. Each component of the particle's velocity is assigned a 30 cm/s a priori uncertainty, which is the same order of magnitude as the escape speeds on Bennu's surface. It was deemed that if the IOD solution could not be trusted at this level, then that IOD solution was not useful as a starting solution. In the vast majority of cases, the total correction from the IOD solution at the filter epoch was less than 50 m, with the data driving the a posteriori uncertainty.

The area-to-mass ratio for each particle was estimated with an a priori constraint set to $\eta = 0.08 \pm 0.1$ m^2/kg, which corresponds to a 0.9-cm particle with 2,000-kg/m^3 density. The constraint allows the solution to readily move close to 0 (representing large particles) but constrains $\eta < 0.38$ m^2/kg (size larger than ~2 mm) at 3 sigma.

The particle trajectories are propagated using a 16×16 spherical harmonic gravity field. Nominally, the gravity field is not estimated. Of the few hundred particles that have been fit, about 20 contain valuable gravity information. These particles were fit simultaneously to produce a single, combined estimate of the gravity field as described in section 5.6 below. This gravity field was then fed back in to the rest of the particle solutions.

Empirical accelerations were modeled as described in section 3.4, and the nodes $\mathbf{a}_i$ of the linearly interpolated accelerations were estimated. We chose a 1-hr spacing between nodes to capture any unmodeled dynamics at finer temporal resolution than the typical particle orbital period. The a priori uncertainty of each node was set to 10^{-11} km/s^2, somewhat more than the net acceleration due to reflected radiation pressure. We believe this choice to be conservative given that the majority of particles, particularly shorter-lived particles, do not require any miscellaneous accelerations, and the set of longer lived particles that do

generally only require accelerations on the order of a few times 10^{-12} km/s^2, which is well below the a priori uncertainty. This results in larger a posteriori uncertainties for the estimated parameters.

The final set of estimated parameters are stochastic corrections to the spacecraft trajectory. The spacecraft trajectory is assumed to be accurate to ±50 cm, 1 sigma, and corrections are estimated in the Bennu-centered radial-transverse-normal (RTN) frame in 1-hr batches, correlated exponentially with a time constant of 4 hours to prevent blatantly discrete, nonphysical jumps. With these settings, we estimate sub-sigma corrections to the spacecraft trajectory at all times.

The empirical accelerations and the estimated corrections to the spacecraft trajectory are in tension with each other in the OD process, and there was the risk that either or both might alias with the gravity field. To characterize these concerns, we performed tests in which we varied the balance of relative a priori uncertainties between the empirical accelerations and spacecraft position errors. Loosening the a priori constraints on the spacecraft trajectory did not effect either the miscellaneous forces or the gravity field and the trajectory corrections remained bounded at <50 cm. Tightening the a priori constraints on the spacecraft trajectory added structure to the residuals and generally increased the magnitude of miscellaneous forces; however, the gravity field remained unaffected.

On the other hand, tightening the a priori constraints on the miscellaneous forces also resulted in structured residuals and caused multimeter corrections to the spacecraft trajectory. In this case GM increased a few sigma; however, this also did not have a large effect on the harmonic coefficients. Moreover, we found no appreciable correlations between the miscellaneous forces and any of the harmonic coefficients when inspecting the estimated covariance matrices. This is not particularly surprising in light of the fact that our gravity estimate (section 5.6) is based on a simultaneous fit of numerous particles. For an individual particle fit, empirical forces could more readily alias with gravity signals, but with multiple particles this risk is significantly diminished because the common gravity field cannot be significantly skewed by the empirical forces of a single particle. And since the empirical accelerations are estimated parameters, any correlation with the gravity field would manifest as increased uncertainty on the gravity coefficients. Thus, the incorporation of empirical accelerations serves to weaken the gravity field estimate in an appropriate way.

To minimize linearization errors associated with the differential correction, both the numerical integration and filtering epochs are chosen to be near the mean of the observation times. This requires that the integration is performed in two legs—a backward leg and a forward leg—the result of which is that the total duration over which nonlinear effects could manifest is halved. This has the primary effect of reducing the number of iterations needed for convergence, and it also allows for the fitting of longer-duration arcs.

4.3. Orbit Linkage

The final stage of the particle orbit determination is the track association, which is the process of determining which tracks belong to the same object and refitting the trajectories accordingly. Linkages were obtained either through *orbit identification* (Milani et al., 2000) by virtue of orbital similarity in cases where both tracks had fitted orbits, or by *attribution* (Milani et al., 2001) if only one track had a successful orbit estimate.

For orbit identification, the best fit trajectories for each track were compared to one another in a statistical sense. For each pair of tracks, the trajectory and uncertainty of both tracks were propagated to their midtime (provided both trajectories exist at this time). The combined Mahalanobis distance, $\mathscr{D}$, was then computed as

$$\mathscr{D} = \sqrt{\delta\mathbf{x}^T P^{-1} \delta\mathbf{x}},$$

where $\delta\mathbf{x} = \mathbf{X}_2 - \mathbf{X}_1$ is the difference between the six-dimensional position and velocity states and $P = P_1 + P_2$, the sum of the mapped covariance matrices, is the combined state uncertainty in both orbits. $\mathscr{D}$ is a direct, scalar measurement of the likeness of two orbits in units of standard deviation. We found that, in general, orbit pairs with $D \lesssim 2$ were in fact the same object.

Then, we performed attribution, which involved propagating a fitted track's trajectory and uncertainty to the midtime of another track, rotating the state uncertainty into the OSIRIS-REx spacecraft's plane of sky, and computing the Mahalanobis distance in the four-dimensional space of right ascension, declination, and their

rates. We computed the observed plane of sky position and velocity at the midpoint via interpolation. This method has the advantage of only requiring one of the two tracks to have a determined orbit, which provided the opportunity for tracks that failed during IOD/OD or tracks that have less than three detections to be linked.

While we relied heavily on the tracks that were formed by linking detections, as described by Hergenrother et al. (2020) and Liounis et al. (2020), we also attributed 861 previously unlinked detections by scanning the entire detection database for sets of unlinked detections that were close to the predicted position for

a given particle. Typically, we would add the new detections to an existing track, though in many cases we formed a new track from the attributed detections. We have so far not gone back to the images to search for detections not in the database. This approach might be occasionally successful, especially for ruling out potentially spurious orbital solutions, but as mentioned in section 2, our detection database is deliberately very complete at the cost of having a low purity.

Once the links were made, the OD and association process was iterated until no further links were found. However, there are likely a few missing links within our catalog, as we know the orbit identification and attribution algorithms are not foolproof. We did perform visual inspections of both the trajectories and the residuals to catch any obvious links that were missed. Most of these were easily fed back into the OD; however, we found a few that we believe to be related that at time of this writing have proved difficult to fit together (e.g., P249 ⇔ P252, P294 ⇔ P303, P289 ⇔ P302, and P31 ⇔ P153). Each of these particle pairs appear to be in remarkably similar orbits and are photometrically consistent, but according to our *orbit identification* tests, they are statistically very different ($\mathscr{D} \gg 10$), and when we try to fit them together, we estimate significantly larger (∼2–10 times) miscellaneous forces than we do in the individual solutions. This may be an indication of an impulsive change in the orbit as would be seen, for example, for fissioning of grains from the particle, but for the present we leave these particles unlinked as we continue to investigate their relationship.

5. Results and Discussion

Our approach has been to estimate a trajectory for each of the 517 tracks that have been visually validated and that have $N_{\mathrm{det}} \geq 3$. From among these, there were a modest number (∼25) of failures in IOD or OD, in many cases because the IOD returned a solution in an erroneous local minimum. Overall, this approach led to successful fits for 390 objects comprising 488 tracks. From among these, we excluded from the following analysis those particles for which we are doubtful that the fit is reliable owing to, for example, a poor fit to the data, a weak orbital solution, or an orbital solution that appears erroneous. More specifically, we considered the fit too poor if the weighted RMS (WRMS) of postfit residuals exceeded unity, and we judged the solution controlled too much by the a priori constraint (and not enough by the data) if the maximum eigenvalue of the 3×3 position covariance matrix was more than 90% of the 250 m a priori constraint. We also excluded cases where particle trajectories appeared nonphysical, for example, cases where the estimated trajectory showed the particle was occulted by Bennu at the time of any detections, or cases that appeared to arrive from infinity. The cases that arrived from infinity did so at low velocities, 1 m/s or slower, and thus are related to Bennu and not interplanetary passersby. Moreover, their orbital geometries were inconsistent with particles that were "blown" back into the Bennu vicinity by SRP. Finally, we excluded several cases where the particle was traveling on a low-eccentricity orbit and unusually close to the spacecraft at the time of observations, which is an a priori unlikely solution that often indicates that the solution is in the wrong local minimum. Together these exclusions removed 77 cases from consideration, leaving 313 particle trajectories for the analysis that follows.

In an external data repository we provide a catalog of these 313 trajectory estimates (Chesley et al., 2019). In what follows, we prepend a "P" to the Object Number designation from this catalog to form an identifier for individual particles. For example "P100" refers to Object Number 100 from the catalog.

Altogether, our 313 particle trajectories are based on 409 distinct tracks and 5,087 detections. For 36 particles, we were able to link multiple tracks to form a larger data set. Most often this consisted of linking only two tracks together, but in seven cases we were able to link six or more tracks, including one case (P2) with

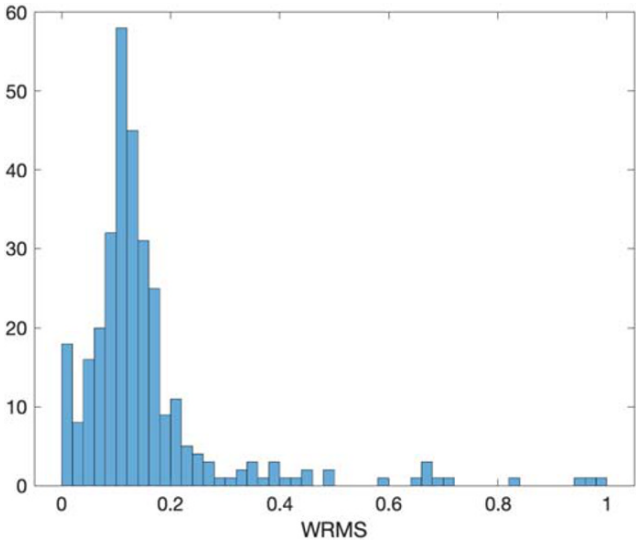

Figure 4. Weighted RMS of postfit residuals for 313 particle trajectory fits.

15 tracks altogether. All told we were able to link a total of 96 additional tracks to existing objects, including a few tracks with only two detections.

Figure 4 depicts the distribution of WRMS for our 313 fits. The distribution is strongly skewed toward 0 and away from the idealized value of unity, indicating that the data are underweighted, which we consider desirable given the presence of systematic errors in the dynamical and observational models, as well as the extraordinary flexibility built into the solution process through the estimation of empirical accelerations and spacecraft position errors (as described in section 4.2). The distribution suggests that some of the fits with WRMS >0.5 may also be spurious. Indeed, while we are confident that the vast majority of our fits are reliable, there are likely a few apparently valid and yet spurious solutions, but given the large data set at hand, this does not compromise the overall analysis. Validating these solutions and incorporating additional data are ongoing efforts.

The observed arc for most particles is fairly short, with 114 particles (36%) having data sets covering <1 hr and only 10 extending over 24 hr in duration. At 5.5 days, P1 has the longest observed arc. The number of detections ranges as high as $N_{\mathrm{det}} = 378$ for P247, and we have 13 particles for which $N_{\mathrm{det}} > 50$ (see Figure 5).

We find that 259 (83%) of our particle trajectories have both ejection and impact within 7 days of the detection set, and hence a finite lifetime. Figure 6 shows the distribution of these cases, among which 80% have lifetime shorter than a day and the median lifetime is 0.23 days. The maximum lifetime is 6.7 days, but we emphasize that for 17% of objects we do not identify an ejection or impact or both, meaning that a lifetime could not be determined. For such cases with an identified ejection or impact, the nominal lifetime would be upward of 7 days, and at least 14 days otherwise. However, most cases with indefinite lifetime are dominated by orbital uncertainties, and we expect that many are in fact relatively short lived. Overall, these results are consistent with the Monte Carlo—like approach taken by McMahon et al. (2020), who found only 10% of their nonrandom samples remained aloft and near Bennu for longer than 7 days.

5.1. Orbital Types

We can categorize our particle trajectories according to their orbital type: suborbital, orbital, or escaping. The key parameter that determines into which category a particles falls is the velocity (magnitude and direction) at ejection. Slower velocities will tend toward suborbital and faster velocities will tend toward escape, with the objects experiencing multiple orbital revolutions falling in between.

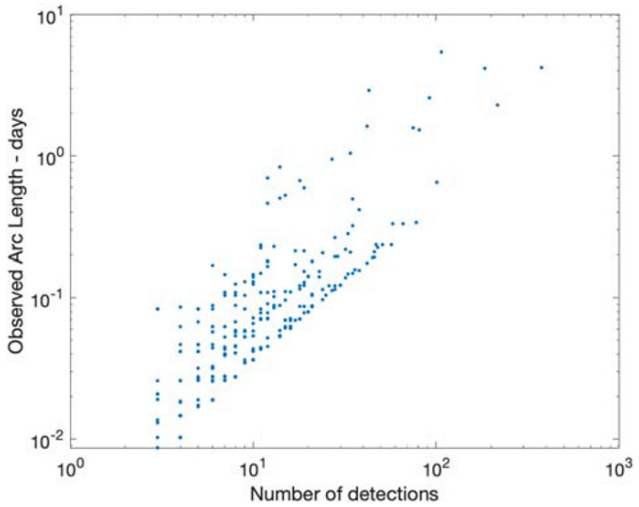

Figure 5. Arc length versus number of detections for particle trajectory fits.

A particle's periapsis radius is necessarily below the surface at ejection, and so under the naive assumption of Keplerian motion about a spherical body, there can be no multirevolution objects. But under a more realistic dynamical model, those objects that gain energy from SRP after ejection can raise their periapsis to a point above the surface within the first revolution. This happens most readily when the velocity at apoapsis is oriented away from the Sun. Thus, in addition to the magnitude of the velocity, the orientation of the osculating orbital ellipse at ejection can be a deciding factor for a particle's fate.

Figure 7 depicts the distribution of ejection velocities, with color coding to indicate the orbital type. Inertial or orbital velocities, which are relative to Bennu in a nonrotating frame, predominantly range from 10–22 cm/s and show a sharp transition in orbital type around 18–20 cm/s, corresponding to the Bennu escape velocity. The sharp drop above the escape velocity presumably reflects a selection effect against particles that do not stay near Bennu for long and therefore are less likely to be observed. In

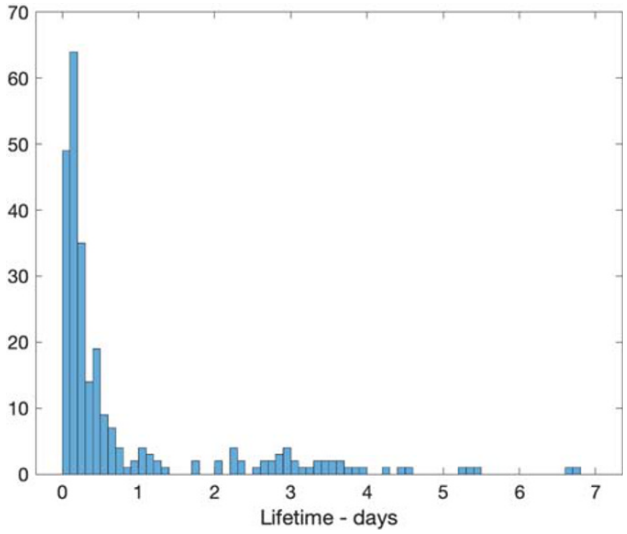

Figure 6. Distribution of particle lifetimes for the 259 particles having both an ejection and impact within 7 days of the mean of the observation times.

contrast to the inertial velocities, surface-relative velocities are smeared by the velocity of the surface (~10 cm/s at the equator), and thus, they range from 4–28 cm/s and show no sharp transition at the surface escape velocity.

5.1.1. Suborbital Particles

About two thirds (204/313) of our particles have suborbital trajectories, meaning that they do not survive their first periapsis passage. The apoapsis radius ranges from ~275 m (only ~40 m above the surface) to >2.5 km, and the lifetimes range from 0.5 to 26 hr. P106 is an outlier with a maximum radius >3 km and lifetime of 90 hr; however, the long life and relatively short data arc (~12 hr) situated near impact leave high uncertainty as to the actual trajectory early in P106's life. Figure 8 depicts examples of suborbital trajectories, including that of P106.

5.1.2. Orbital Particles

One fifth (63/313) of cases are quasi-elliptical orbits with more than one revolution around Bennu. Figure 9 depicts examples of orbital trajectories. This category can have as few as two revolutions, and in a few cases upward of 10, with P2 having the most at 16 revolutions (Figure 9). However, there are a number of objects that could have longer lifetimes, given that they do not contact the surface over our 14-day scan period, but orbital uncertainty dominates these cases and so we presume that most of them have much shorter lifetimes. In a number of cases, the nature of the trajectory, in particular the number of revolutions, is unknown. P192, for example, could actually be suborbital (Figure 9) given that it has the minimum number of detections and a very low altitude at its first periapsis passage, thus demonstrating the potential for ambiguity in assigning the orbital type in near-transition cases.

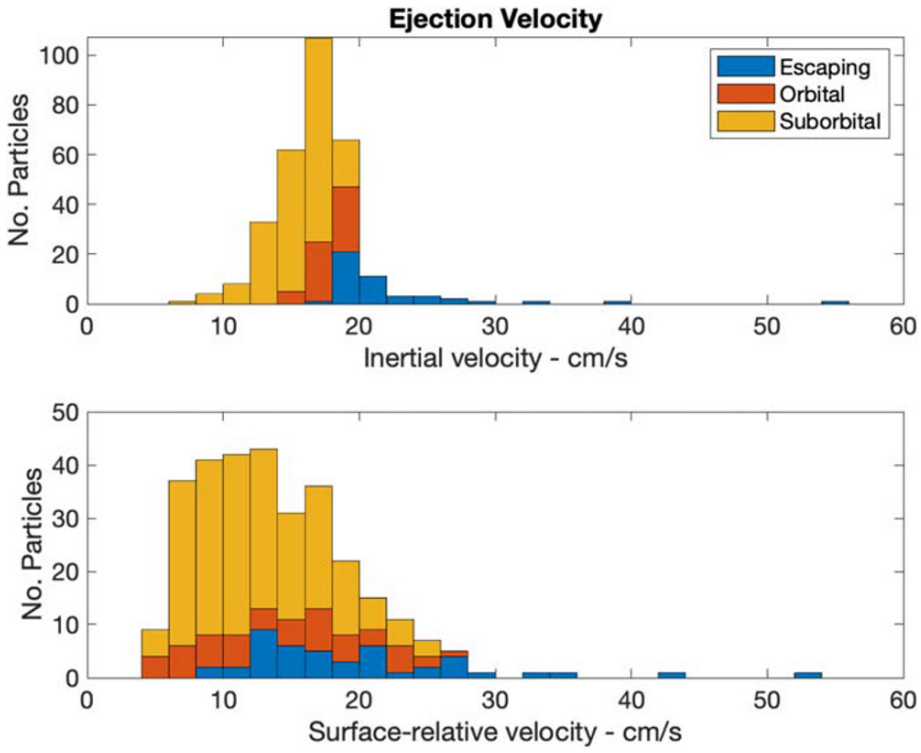

Figure 7. Velocity magnitude at ejection. Upper panel: orbital velocity. Lower panel: surface-relative velocity. Color coding is according to orbital type.

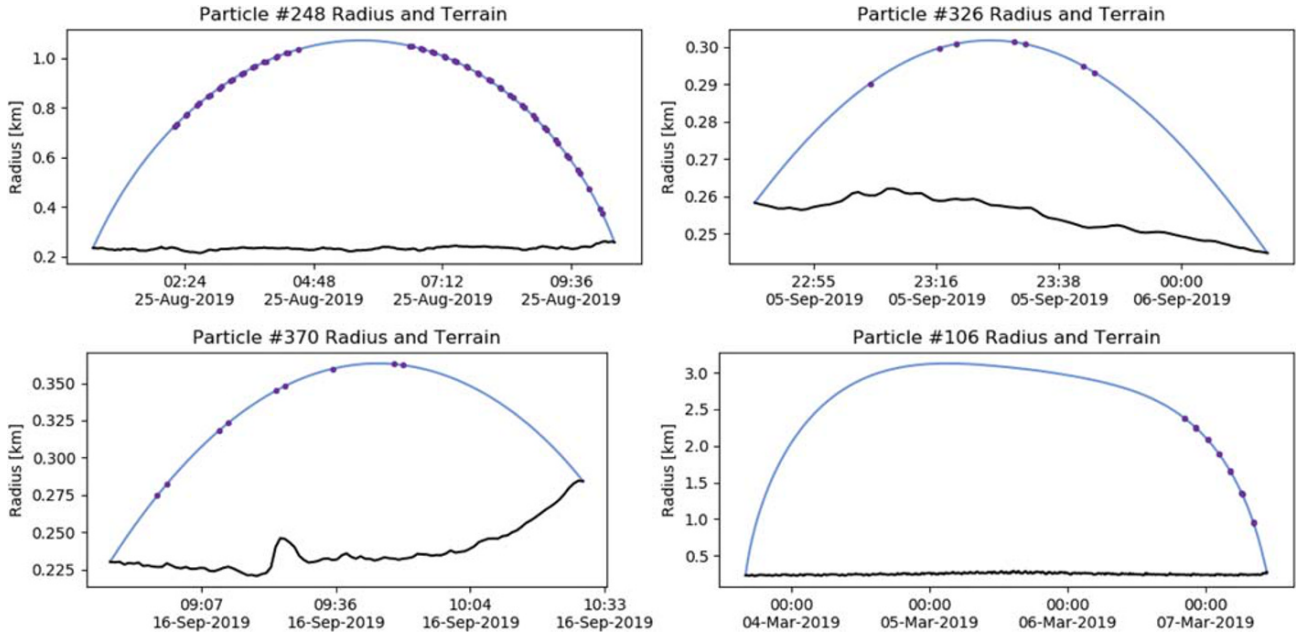

Figure 8. Examples of suborbital trajectories. The blue curves depict the orbital radius of the particle as a function of time, with dots marking the times of observations. The black curves represent the terrain, that is, the radius of Bennu at the subparticle point.

5.1.3. Escaping Particles

About one seventh (46/313) of the particle trajectories are hyperbolic with respect to Bennu. Figure 10 depicts examples of escaping trajectories. With few exceptions, these are all direct escape following ejection. One of these exceptions is P7, which may have escaped after the first periapsis passage, or may have returned for a second close periapsis passage before escape (Figure 10). P137 (Figure 10) was lofted as a part of the major ejection event on 19 January 2019 and spent a few days weakly bound to Bennu before probably being swept away by SRP.

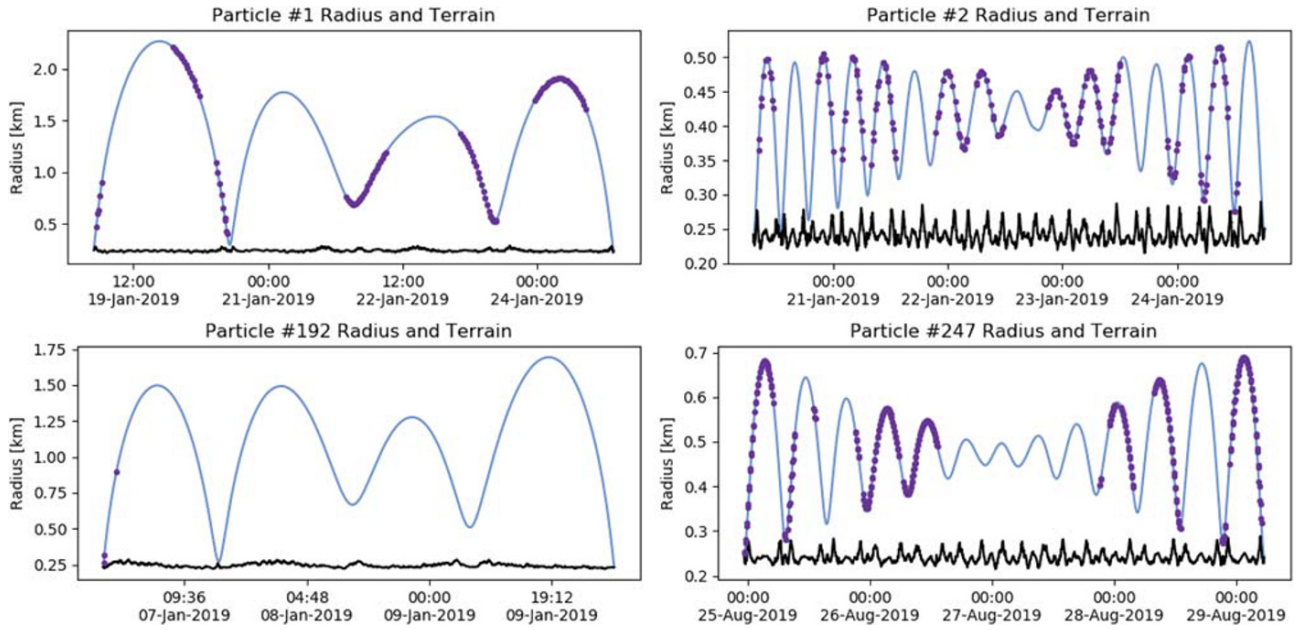

Figure 9. As in Figure 8, but for orbital trajectories.

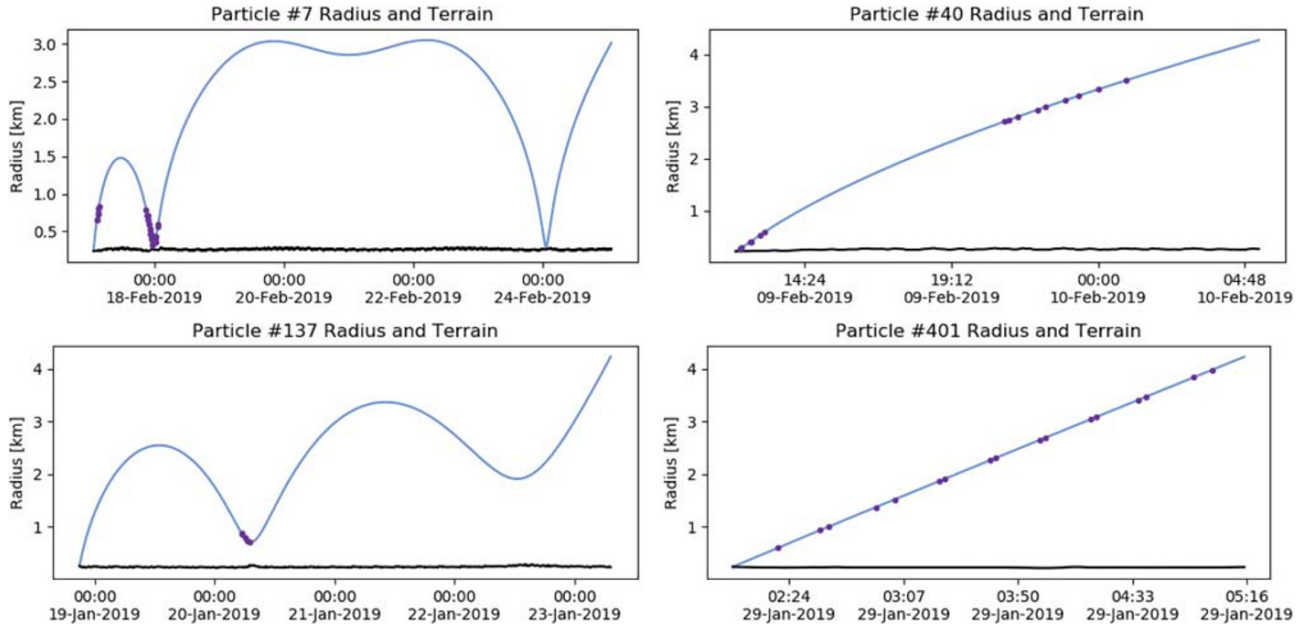

Figure 10. As in Figure 8, but for escaping trajectories.

5.1.4. Hyperbolic Flyby Particles

There is the possibility that particles could be ejected on near-parabolic or weakly hyperbolic orbits toward the Sun, in which case SRP could slow and even reverse the particle's escape, sending it back to the near-Bennu environment. McMahon et al. (2020) have identified this type of behavior in Monte Carlo-like simulations and conclude that it can afford a very long lifetime in the Bennu environment in some cases. In this scenario, given that linking the returning particle back to its original ejection would likely be infeasible, the particle would appear as a low-velocity hyperbolic flyby (or impactor). A small angle between the Sun direction and the particle's inbound asymptote should be diagnostic of this type of trajectory. We have not seen such cases in the solutions to date, which is not particularly surprising given that the analysis by McMahon et al. (2020) found only 0.05% of their escaping samples were returned to within 5 km of Bennu. With our smaller sample size, we would not expect to see any such cases. Although our initial sampling of 390 particles included a number of nominally hyperbolic flybys at speeds below 0.5 m/s, we are doubtful that any of them are credible. Many are likely associated with a direct ejection, given that the orbital uncertainty readily puts the particles below the surface at periapsis, and the inbound asymptotes are not oriented such that SRP would account for the returns. Some others are likely errant solutions in a local minimum given that the Sun is not situated in a direction to explain a hyperbolic flyby. We treat all such cases as spurious and neglect them in our analysis.

5.2. Particle Size

The radiation pressure acting on the particles has a significant effect on the trajectories, so much so that the area-to-mass ratio η can be estimated with good precision. Again, we are only able to estimate the combined direct and reflected radiation pressure term $\eta' = (1 + \frac{4}{9}\mathscr{A}_{\mathrm{Bond}})\eta$, where we assume $\mathscr{A}_{\mathrm{Bond}} = 0.016$ to derive η. The estimated values of η and the associated formal uncertainties σ_η are available in our catalog (Chesley et al., 2019). For the purposes of our discussion here, we limit the analysis to particles for which the a posteriori uncertainty σ_η is not substantially controlled by our a priori uncertainty constraint of $\sigma_{\eta_{\mathrm{prior}}} = 0.08\,\mathrm{m}^2/\mathrm{kg}$. Thus, we require $\sigma_\eta < 0.8\ \sigma_{\eta_{\mathrm{prior}}}$ to ensure that the result is driven by the data. We also drop those cases with low significance estimates, ensuring that the η estimate has an SNR $= \frac{|\eta|}{\sigma_\eta} > 2$. Thus, we consider 130 estimated values of η, which we plot in Figure 11. Many of the estimates have very low formal uncertainties;

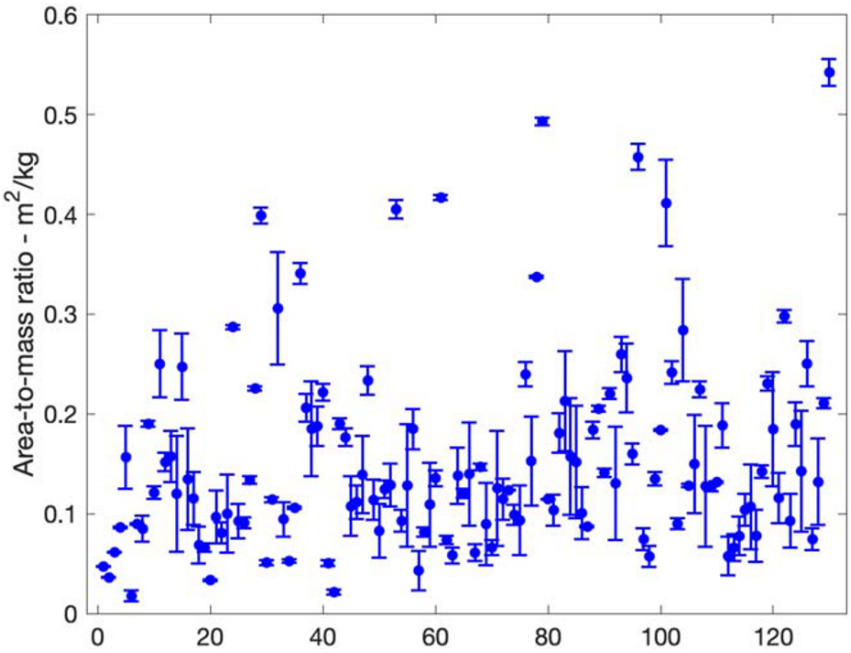

Figure 11. Area-to-mass ratio (η) for 130 particles with well-constrained estimates.

for example, 16 cases have SNR > 100, indicating a strong effect on the trajectory that is plainly evident in the observations.

Whatever the means of ejection, it is reasonable to assume that a nonnegligible fraction of a particle's kinetic energy is rotational in nature. If we assume that the kinetic energy partition allows only 10% of the kinetic energy to stem from particle rotation, we still have a very rapid rotation rate, ~0.3-s rotation period for a typical orbiting particle in simple rotation. But simple rotation is unlikely, and thus, the particles should be rapidly tumbling. The area-to-mass ratios that we quote here should be representative of mean values over a time interval many orders of magnitude longer than the rotation period.

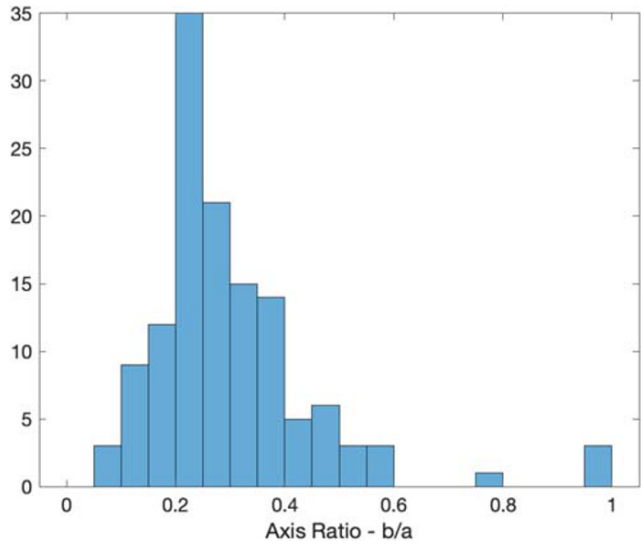

Figure 12. For 126 particles having reliable area-to-mass ratios and absolute magnitude estimates, the distribution of estimated particle axis ratios $b/a<1$ for oblate ellipsoids of revolution based on estimated area-to-mass ratios and absolute magnitudes (Hergenrother et al., 2020), assuming $\mathscr{A} = 4.4\%$ and $\rho = 2{,}000\ \mathrm{kg/m^3}$.

To put these values of area-to-mass ratio into context, we translate them to diameter D. For spherical particles,

$$D_\eta = \frac{3}{2\rho\eta}.$$

We take $\rho = 2{,}000\ \mathrm{kg/m^3}$ based on presumed Bennu meteorite analogs (Clark et al., 2011; Hamilton et al., 2019). This leads to a set of diameters that range over 0.13–4.1 cm with median 0.56 cm, and that can be compared with those derived from particle photometry and using similar assumptions. To this end, we also define the diameter D_H derived from absolute magnitude H, again assuming spherical particles, as

$$D_H = 1329 \times 10^5\ \mathrm{cm} \cdot \frac{10^{-H/5}}{\sqrt{p_V}}.$$

Hergenrother et al. (2020) shows that assuming the Bennu albedo of 4.4% leads to a discrepancy in D_H compared to D_η, with the absolute magnitudes pointing to larger particles than the area-to-mass ratios by a median factor 1.5×. Hergenrother et al. (2020) go on to show that the discrepancy can only be reconciled by assuming a significantly

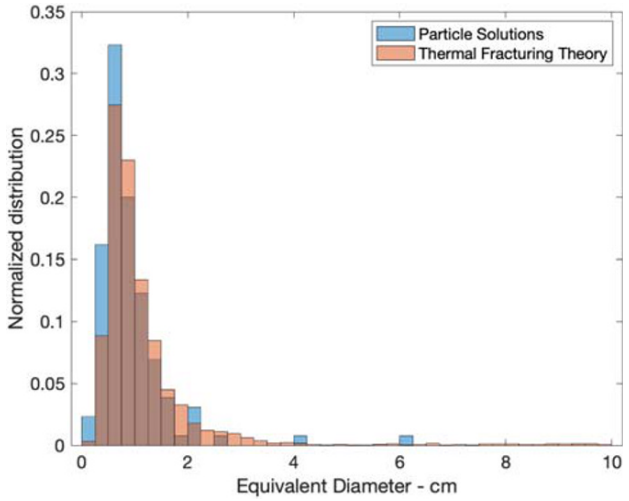

Figure 13. Distribution of volume-equivalent spherical diameters for our particle solutions (blue bars) based on the combined information from absolute magnitude (Hergenrother et al., 2020) and area-to-mass ratio, and assuming $\mathscr{A} = 4.4\%$ and $\rho = 2{,}000\ \mathrm{kg/m^3}$. For comparison, the plot also depicts the size distribution of thermally fractured fragments (red bars) as described in the text according to the exfoliation model by Molaro et al. (2020).

larger albedo (10.5%) or a significantly lower mass density (1,340 $\mathrm{kg/m^3}$) for the particles, which they argue would be challenging to explain.

To resolve this apparent discrepancy, we drop the assumption of spherical particles and assume instead an ellipsoid of revolution having semiaxes $a{\times}a{\times}b$ and derive the axis ratio $p{=}b/a$. We continue with the assumption of rapidly tumbling particles and obtain the average cross-sectional area $\bar{A} = \pi a^2 f(p)$, where the function $f(p)$ is defined and derived in A1. With this then

$$\eta = \frac{\bar{A}}{M} = \frac{3pf(p)}{4\rho a} \Rightarrow a = \frac{3pf(p)}{4\rho\eta}. \quad (1)$$

On the other hand, the photometric estimate of the size is purely dependent on the cross section and so

$$\bar{A} = \frac{\pi}{4}D_H^2 \Rightarrow a = \frac{D_H}{2\sqrt{f(p)}}. \quad (2)$$

By combining Equations 1 and 2, we can simultaneously determine the semimajor axis and the axis ratio of the particle, given an estimated area-to-mass ratio and absolute magnitude and assumed albedo and density. We can generally find two solutions: one corresponding to $p < 1$, that is, an oblate shape, and one for $p > 1$, that is, a prolate shape. We selected the former, which would imply a flake-like shape for the particles, consistent with the shapes of fragments seen in laboratory impact experiments (e.g., Capaccioni et al., 1984; Michikami et al., 2016). Figure 12 shows the resulting values of p for $\mathscr{A} = 4.4\%$ and $\rho = 2{,}000\ \mathrm{kg/m^3}$. The distribution has a range from 0.07–1.0 and median 0.27. These results are in rough agreement with laboratory impact experiments, which tend to find axis ratios ranging from 0.2–1 with median ~0.5 for catastrophically disrupting impacts (Capaccioni et al., 1984). However, Michikami et al. (2016) find that subcatastrophic disruption impacts lead to lower axis

Table 2
Summary of Candidate Event Times, Locations, and Local Solar Times (LST)

Time (UTC)	Longitude	Latitude	LST	N_{part}	Particle numbers
2019-01-19 00:53:43 ± 3 s	335.383° ± 0.4 m	19.925° ± 0.9 m	16:39:41	14	126, 127, 129, 135, 136, 173, 174, 176, 182, 183, 196, 200, 202, 203
2019-01-26 09:26:55 ± 61 s	11.369° ± 1.4 m	−25.004° ± 3.0 m	22:00:25	2	175, 181
2019-02-11 23:27:45 ± 4 s	59.739° ± 0.3 m	15.065° ± 0.7 m	18:06:50	6	51, 54, 162, 165, 167, 169
2019-02-15 18:52:38 ± 20 s	55.707° ± 1.1 m	8.017° ± 0.7 m	00:50:13	3	80, 83, 84
2019-08-16 10:51:59 ± 74 s	248.834° ± 1.5 m	32.606° ± 2.6 m	20:12:26	2	29, 228
2019-08-23 10:36:57 ± 33 s	196.423° ± 1.1 m	48.741° ± 10.0 m	18:07:17	2	315, 316
2019-08-28 18:35:28 ± 195 s	74.046° ± 11.6 m	42.728° ± 17.0 m	05:06:20	2	263, 267
2019-09-05 22:44:34 ± 33 s	319.315° ± 2.3 m	−10.689° ± 3.9 m	13:34:56	2	326, 327
2019-09-13 22:40:36 ± 4 s	20.595° ± 1.5 m	−65.379° ± 0.3 m	10:13:26	5	343, 344, 345, 353, 354
2019-09-14 04:25:25 ± 25 s	181.255° ± 1.2 m	32.266° ± 1.8 m	05:03:00	2	359, 360

Note. Location is given in degrees of longitude and latitude, while the associated uncertainties are tabulated in meters to better convey the scale of the spatial uncertainty. The number of particles N_{part} used in the estimate and the catalog numbers of the associated particles are also listed. Dates are formatted as YYYY-MM-DD.

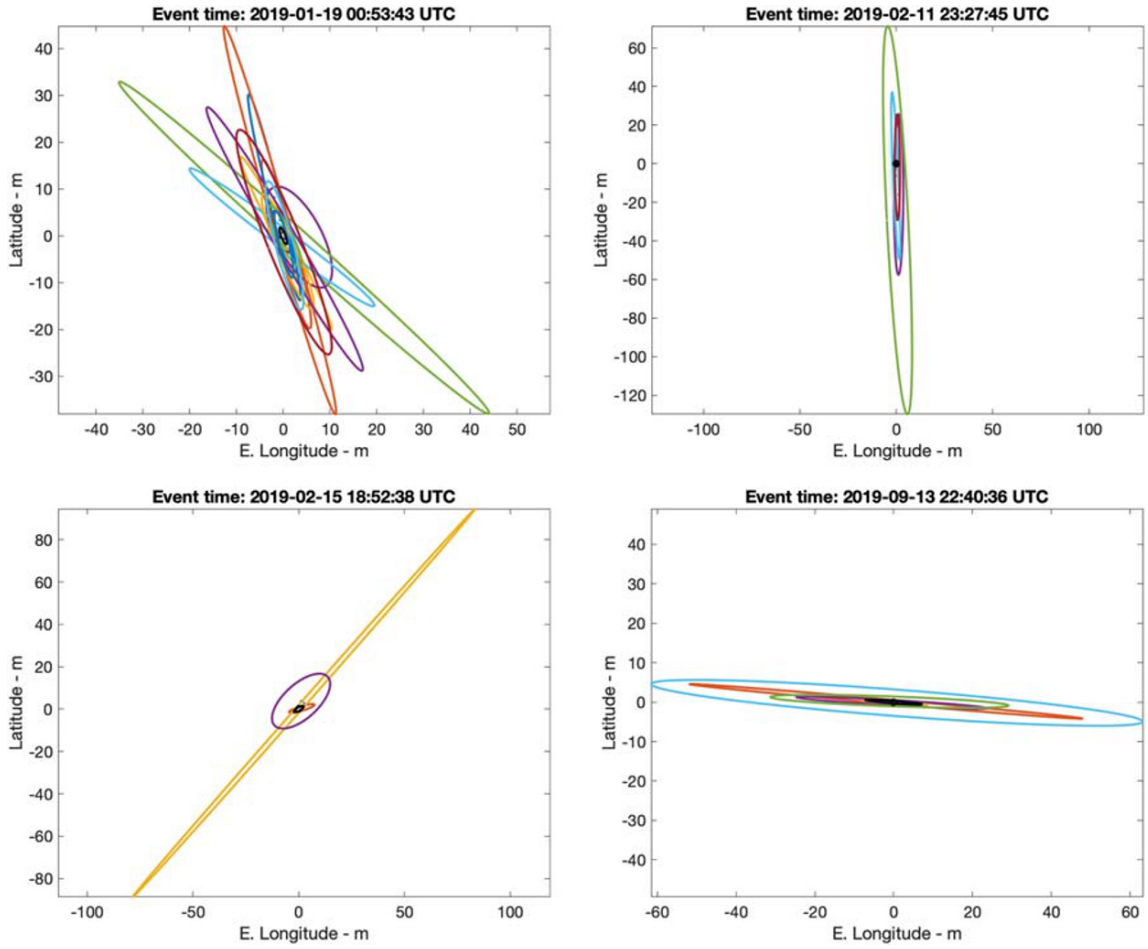

Figure 14. Ejection location estimates for the four events for which we have associated three or more particles (Table 2). In each case the black ellipse represents the weighted mean and uncertainty of the individual particle ejection estimates, while the colored ellipses depict the location and uncertainty of the individual particle ejection estimates. All ellipses indicate the 3-sigma confidence region.

ratios, with the ratio of the smallest to largest axes of fragments being as small as 0.2 in the mean, very much in accord with our distribution. If there is a discrepancy between our distribution of p and those found from impact experiments, it may be a manifestation of measurement or modeling errors, but with so many samples at hand it could as well be an indication that our particles are not exclusively created by hypervelocity impacts.

Some of the extreme values for the axis ratio p could be caused by the simplifying assumptions in our derivations. Instead of a uniformly distributed orientation of the particle, we could have a flake that is experiencing only a moderate wobbling, and in that case the spacecraft might see mostly the face of the particle while the Sun might see mostly the edge of the particle (or vice versa). This scenario would violate our averaging assumptions and would imply a less extreme axis ratio. Moreover, some of the outliers could be simply explained by the formal uncertainties in η and H. The key point here is that accounting for a nonspherical shape can lead to consistent size estimates from photometry and SRP solutions.

Figure 13 plots the distribution of diameters for volume-equivalent spheres $D = 2a\sqrt[3]{p}$, which has a range 0.22–6.1 cm with median 0.74 cm, somewhat larger than the distribution for D_η.

One candidate mechanism for driving particle ejection from the asteroid surface is fatigue from diurnal thermal cycling (Lauretta et al., 2019; Molaro et al., 2020). Fatigue-driven exfoliation, the flaking of thin layers of material from boulder surfaces, is observed widely across Bennu (Lauretta et al., 2019) and known to drive the mobilization of disaggregated rock fragments in terrestrial environments (Collins et al., 2018). Molaro

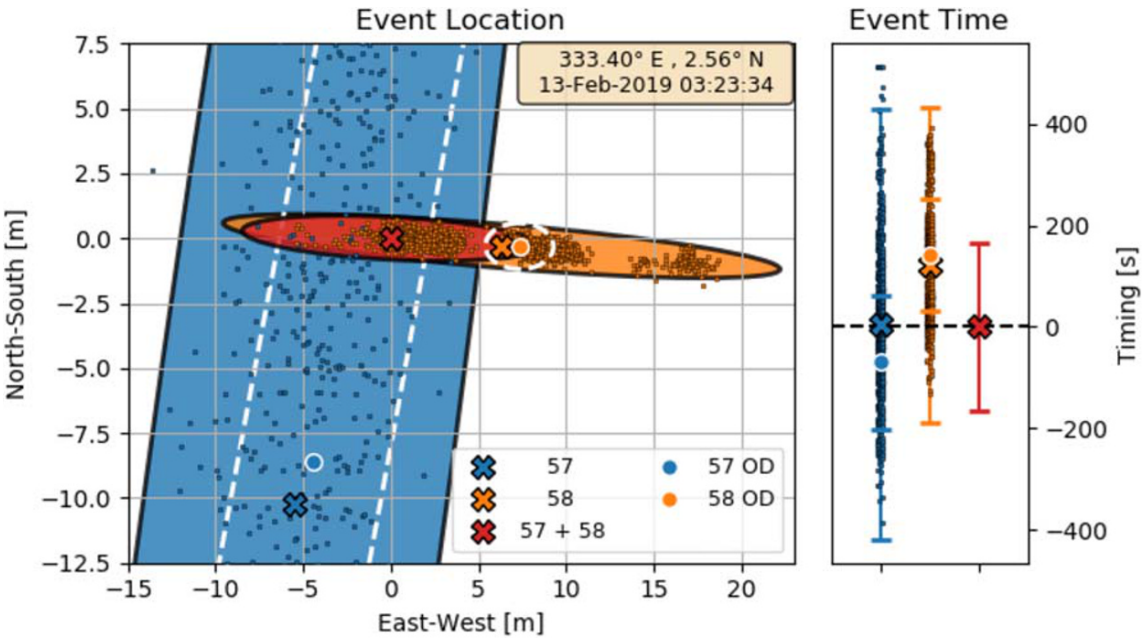

Figure 15. Bounce footprint (left) and timing (right), demonstrating agreement between the impact of P57 and ejection of P58. The blue and orange dots denote the propagated Monte Carlo samples. The blue and orange ellipses (errors) are 3 sigma and are computed from the empirical covariances of the samples. The crosses indicate their respective means, and the joint solution is shown in red. The timing is centered about the joint solution. The formal OD solutions are shown in white.

et al. (2020) developed a model to predict the characteristic spacing of exfoliation cracks in Bennu's boulders and quantify the particle sizes and ejection speeds that may result from an exfoliation event. The model assumes that surface-normal exfoliation layers are disaggregated into equal-sized cubes, each the size of the layer thickness. Here, however, we assume that the exfoliation layer is decomposed into flakes of thickness $2b$ with axis ratio $p = b/a$

distributed according to Figure 12. This allows a range of particle sizes and volume-equivalent spherical diameters. With these assumptions, Figure 13 compares the size distribution of our particles with that produced by exfoliation layers in a 1-m boulder (Molaro et al., 2020). Although the mass that may be ejected during a given exfoliation event is not well constrained, the shape and peak diameter of the size distribution of thermally fractured fragments provides a good match to our results. This reinforces the hypothesis that particles ejected from Bennu are fragments arising from diurnal thermal cycling on the surface.

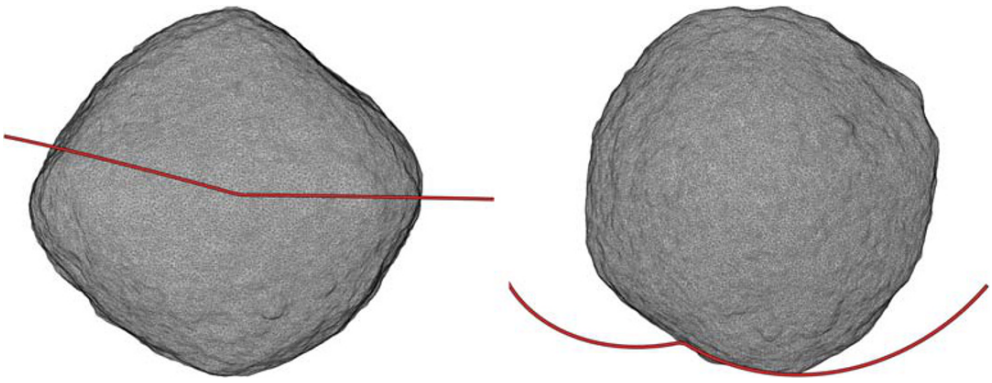

Figure 16. Orbital diagrams of the ricocheting particle. The left view is from directly above the event location at 333°E and 2.5°N, and the right view is from above Bennu's north (+z) pole. The shape is rendered at the event time. The plotted trajectories span 2 hr in total, centered on the bounce time. The trajectory is traversing from left to right in both views, and Bennu's pole is pointing up on the left and toward the viewer on the right.

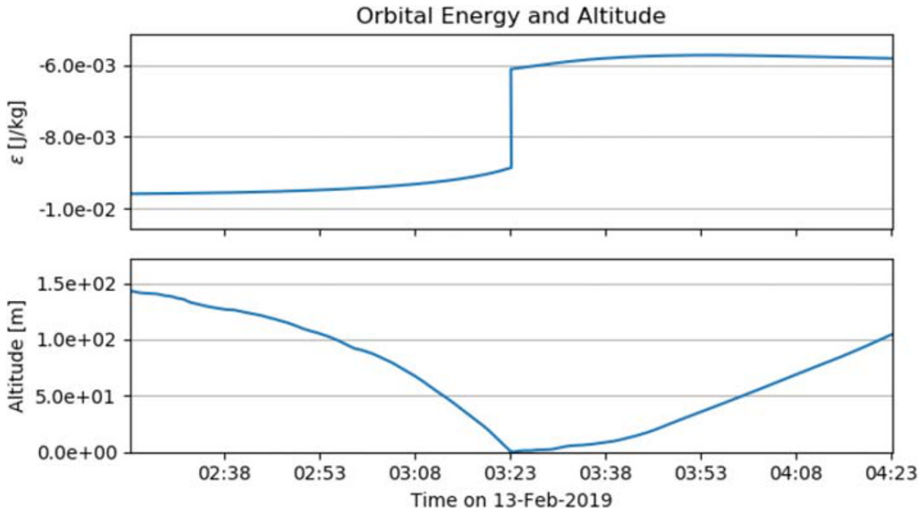

Figure 17. Specific orbital energy (top) and altitude (bottom) of P57 before the bounce and P58 after.

5.3. Concurrent Ejection Events

We scanned our particle catalog for particles that were ejected at nearly the same time and location, which represent *ejection events*. Our orbit estimation approach is complementary to, but independent of, other event analyses, some of which are generally more robust with few detections. For example, Pelgrift et al. (2019) applied kinematic constraints and detailed image processing to characterize ejection events on 6 January, 19 January, and 11 February 2019, among others. In a related effort, Leonard et al. (2020) fitted dynamical orbits with the constraint that all particles in a given event were ejected at a common time and location, which could be estimated. For the present work, we do not enforce the notion that particles from ejection events emanate from a single surface location during the orbit estimation process. Rather, we use the similarity of ejection circumstances to identify candidates that may be associated with an event. After selecting a set of candidates, outliers from the weighted mean are culled (at >2 sigma) until reaching a final set. Table 2 lists the cases for which at least two particles are consistent with a common ejection. Figure 14 depicts the individual particle ejection estimates along with the weighted mean of each case.

Table 3
Detailed Information on the Orbital and Physical Characteristics of P57 and P58, as Well as the Circumstances of the Associated Bounce

Parameter	P57	P58
Propagation time ($\lvert t_{\text{filter}} - t_{\text{event}} \rvert$)	91 min	93 min
Number of observations	7	24
Area-to-mass ratio	0.09 ± 0.09	0.053 ± 0.003
Absolute magnitude[a]	42.82 ± 0.44	42.35 ± 0.5
Orbital inclination[b]	17°	3°
Orbital semimajor axis[b]	0.25 km	0.41 km
Orbital eccentricity[b]	0.62	0.29
Inbound/outbound elevation	67°	20°
Inbound/outbound velocity mag. (body frame)	9.48 cm/s	5.48 cm/s
Inbound/outbound velocity mag. (inertial)	14.03 cm/s	15.89 cm/s
Bounce epoch	2019-02-13 03:23:34 ET ± 55 s	
Bounce longitude	333.4° ± 0.6°	
Bounce latitude	2.6° ± 0.1°	
Bounce local solar time	00:22:35 ± 340 s	
Change in kinetic energy	+2.68 ± 0.16 mJ/kg	
Coefficient of Restitution[c]	0.57 ± 0.01	

[a]Hergenrother et al. (2020). [b]Based on osculating orbit at filter epoch. [c]Assuming single bounce, no mass loss.

Two of our events (19 January and 11 February) were previously characterized by Lauretta et al. (2019). In both cases, results compare reasonably well, though the ejection latitudes for the 11 February event differ by 5°, well outside stated uncertainties. As indicated in Figure 14, some particles from the 11 February event have large latitude uncertainty, though some are much better constrained. We note again that our ejection uncertainty estimates are based on the formal covariance and do not account for surface topography. As seen in the following section for P57 and P58, this simplified uncertainty approach can be reasonably accurate for ejections with steeper trajectories (i.e., high elevation angle velocity), whereas the location and probability distribution for shallower ejections depend heavily on the local topography. The implication is that the uncertainties given in Table 2 may in some cases be optimistic.

5.4. Ejections Spawned by Impacts

On 13 February 2019, a particle was observed ricocheting off of Bennu's surface. During our analysis we were purposefully monitoring for such a possibility, and as a result, we found that the impact time and location of P57 was suspiciously close to the ejection time and location of P58. The location of the contact was on the dark side of Bennu at LST of ~00:30 and took place about an hour after the last image of P57 was taken and

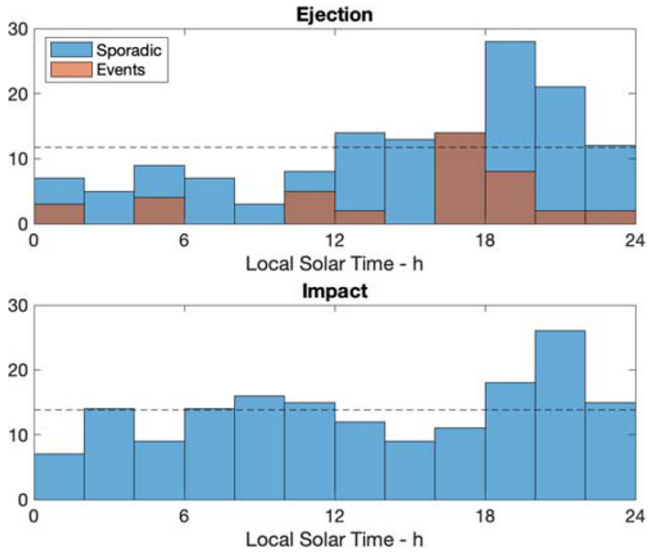

Figure 18. Distribution of local solar time (LST) at ejection (upper panel) and impact (lower panel). For ejections, we plot the histogram of ejections associated with events separate from singleton ejections, which we term sporadic. As reference, the dashed line marks the uniform distribution, given the total number of sporadic ejections (top) and impacts (bottom).

about an hour before the first image of P58 was taken. Their nominal impact and ejection locations were separated by ∼15 m on the surface and ∼3 min in time, which corresponded to a three-dimensional Mahalanobis distance of ∼6 sigma when using the mapped covariances output from the OD process.

However, we suspected the formal OD uncertainties to be optimistic, in which case the statistical agreement would potentially be much greater. In particular, the timing and along-track uncertainties did not fully account for Bennu's terrain, which is extremely rugged. This is a potentially large and nonlinear source of additional uncertainty that will preferentially affect trajectories that intersect at shallow elevation angles. This led us to conduct a Monte Carlo analysis in an attempt to capture the full nonlinear uncertainty. For

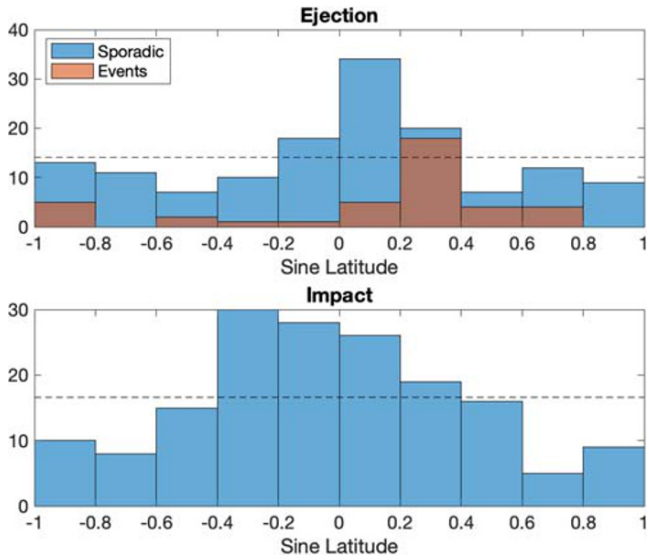

Figure 19. Latitudinal distribution of ejections (upper panel) and impacts (lower panel). As in Figure 18, we plot the sporadic and event-related ejections separately, and the dashed line marks the uniform distributions (sporadic for ejections), which here correspond to a uniform area-wise distribution on a sphere.

Table 4
The 20 Particles Used for Our Gravity Estimate, With the Number of Detections N_{det}, the Data Arc (Duration of the Observed Data Set), and the Lifetime

Particle No.	N_{det}	Data arc (d)	Lifetime (d)	a (km)	e	i (deg)
1	107	5.45	5.79	1.05	0.27	88
247	378	4.23	4.26	0.49	0.13	87
2	185	4.17	4.45	0.40	0.11	83
41	43	2.92	5.35	1.29	0.52	14
3	92	2.58	2.65	0.49	0.12	15
303	217	2.30	2.91	0.44	0.13	29
213	42	1.63	3.30	0.88	0.53	165
4	75	1.58	2.30	0.41	0.17	128
273	81	1.53	2.39	1.34	0.76	17
188	34	1.05	1.12	0.48	0.04	2
289	101	0.65	3.68	0.55	0.39	5
302	35	0.50	3.45	0.53	0.50	7
252	78	0.34	2.37	0.59	0.11	83
248	58	0.33	0.40	0.58	0.87	130
15	66	0.33	0.47	0.61	0.72	1
210	35	0.32	0.33	0.49	0.96	75
50	33	0.28	0.44	0.59	1.00	111
16	47	0.24	0.27	0.45	0.59	16
285	46	0.19	0.21	0.38	0.78	32
269	45	0.19	0.23	0.41	0.43	5

Note. For reference, the approximate semimajor axis a, eccentricity e, and inclination i at the mean epoch of the observations are also listed. The table is sorted by data arc in descending order. In this table, the seven cases with a lifetime shorter than a day are well-observed suborbital trajectories.

both P57 and P58, the correlated estimated covariances were sampled 1,000 times at the filter epoch (the midtime of their respective observations), and each sample was propagated to the surface. The results are shown in Figure 15. The primary driver in the difference in uncertainty between the P57 and P58 solutions is the difference in number of observations: P57 appeared in 7 images and P58 appeared in 24 images.

The first obvious trend to point out is the markedly non-Gaussian nature of P58's samples. P58 departs at a fairly shallow angle of ~20°, meaning that trajectory errors consistent within the formal uncertainties will lead to surface intersections at different points that appear outside of the uncertainty because the samples will collide with different rocks or features. This leads to three groupings in the possible ejection point spread out in the along-track direction. P57, on the other hand, impacts at a much steeper angle of ~67°. Consequently, the formal OD covariance much more accurately captures the Monte Carlo dispersions because the shape intersection is less sensitive to the topography. In terms of Figure 15, P57's along-track error is roughly normal to the page on the left plot and appears primarily as the timing uncertainty in the right plot.

The dispersions in Figure 15 alone are not enough to claim that P57 and P58 are in fact the same object. It is also vitally important to check that the inbound and outbound orbital velocities are dynamically consistent. In Bennu's rotating frame, we would expect the magnitude of the outbound velocity to be smaller than the magnitude of the inbound velocity, and for the change in direction to make sense physically. In other words, we would expect to find a coefficient of restitution, COR, <1 and the arrival and departure elevation angles to be >0. COR < 1 is a hard dynamical constraint, provided the absence of any external forces at the moment of impact (such as fission or outgassing), and the departure elevation condition is met trivially for both objects (otherwise they would not impact/eject). Although the change in direction is captured implicitly in the COR, we also performed visual inspections of the trajectories.

The orbits are plotted in Figure 16. The orbits shown were hand-picked from the set of Monte Carlo samples in Figure 15 to be near the joint solution (discussed later in this section) so they appear continuous in both space and time. The most powerful way to view this is via animation (see Chesley et al., 2019), which captures the relative velocities of the orbits and Bennu's surface. Even so, Figure 16 tells the tale quite well when combined with the ricochet statistics in Table 3. When inspecting the inbound and outbound velocities in Bennu's rotating frame, we find that the outbound velocity is in fact smaller than the inbound, yielding a COR estimate of ~0.57. This value assumes that the event was a single bounce (rather than impact, roll, relaunch, or multiple bounces), and we are unable to say with certainty whether any mass was lost during impact. The inertial velocities also tell an interesting story, namely, that the departing velocity is higher than the arrival velocity. This is because Bennu's surface is traveling faster in inertial space than the velocity of the inbound particle, meaning that Bennu literally kicks the particle back into orbit. This effect is enhanced by the fact that the bounce point is near the equator, where Bennu's surface speed is greatest. As a result, the collision reduces the inclination from 17° to 3°, meaning that the postbounce velocity vector is indeed strongly aligned with Bennu's surface velocity, consistent with the idea that Bennu kicked the object back into orbit. The bounce results in a net energy transfer from Bennu to the particle of ~2.7 mJ/kg, shown graphically in Figure 17. Taken together, the energy transfer leads to an orbit with increased semimajor axis, reduced eccentricity, and reduced inclination (Table 3). This illustrates the fascinatingly complex dynamical environment around small bodies.

Now, based on the dispersions in Figure 15 and the dynamical feasibility shown in Table 3, we can say with high confidence that P57 and P58 are the same object. This conclusion is reinforced by the agreement in absolute magnitude (Table 3) for the two particles reported by Hergenrother et al. (2020). The P57

Table 5
Estimated Spherical Harmonic Coefficients (Normalized) With Uncertainty

Coefficient	Estimated Value	Shape Value	SNR	Deviation (relative)	Deviation (sigma)
J_2	$1.926\times10^{-2}\pm5.2\times10^{-5}$	1.881×10^{-2}	370.4	0.02	8.70
$C_{2,2}$	$3.06\times10^{-3}\pm5.3\times10^{-5}$	3.55×10^{-3}	58.2	−0.14	−9.23
$S_{2,2}$	$-1.09\times10^{-3}\pm1.1\times10^{-4}$	-7.85×10^{-4}	10.3	0.39	−2.90
J_3	$-1.22\times10^{-3}\pm7.9\times10^{-5}$	-1.30×10^{-3}	15.5	−0.06	1.00
$C_{3,1}$	$8.15\times10^{-4}\pm2.9\times10^{-5}$	1.01×10^{-3}	28.0	−0.19	−6.66
$S_{3,1}$	$-5.43\times10^{-4}\pm4.3\times10^{-5}$	-3.44×10^{-4}	12.5	0.58	−4.59
$C_{3,2}$	$-9.35\times10^{-4}\pm4.6\times10^{-5}$	-7.25×10^{-4}	20.5	0.29	−4.61
$S_{3,2}$	$-5.38\times10^{-4}\pm4.9\times10^{-5}$	-7.41×10^{-4}	11.0	−0.27	4.17
$C_{3,3}$	$1.17\times10^{-3}\pm6.0\times10^{-5}$	1.19×10^{-3}	19.5	−0.02	−0.39
$S_{3,3}$	$-3.1\times10^{-4}\pm8.3\times10^{-5}$	-2.8×10^{-4}	3.7	0.13	−0.42
J_4	$-6.50\times10^{-3}\pm7.1\times10^{-5}$	-6.39×10^{-3}	91.4	0.02	−1.44
$C_{4,1}$	$-8.82\times10^{-4}\pm5.8\times10^{-5}$	-8.98×10^{-4}	15.3	−0.02	0.28
$S_{4,1}$	$-5.8\times10^{-4}\pm6.0\times10^{-5}$	-6.8×10^{-4}	9.6	−0.15	1.68
$C_{4,2}$	$-8.71\times10^{-4}\pm5.5\times10^{-5}$	-8.29×10^{-4}	16.0	0.05	−0.77
$S_{4,2}$	$-8.4\times10^{-5}\pm6.5\times10^{-5}$	-8.1×10^{-5}	1.3	0.03	−0.04
$C_{4,3}$	$-7.6\times10^{-5}\pm6.8\times10^{-5}$	-9.6×10^{-5}	1.1	−0.20	0.29
$S_{4,3}$	$-3.9\times10^{-4}\pm6.3\times10^{-5}$	-4.4×10^{-4}	6.1	−0.13	0.90
$C_{4,4}$	$7.7\times10^{-4}\pm1.6\times10^{-4}$	6.7×10^{-4}	4.9	0.15	0.65
$S_{4,4}$	$2.25\times10^{-3}\pm8.5\times10^{-5}$	2.24×10^{-3}	26.5	0.00	0.04
J_5	$6.7\times10^{-5}\pm1.0\times10^{-4}$	1.2×10^{-4}	0.7	−0.42	−0.47
$C_{5,1}$	$-3.5\times10^{-4}\pm8.4\times10^{-5}$	-3.5×10^{-4}	4.2	0.00	−0.00
$S_{5,1}$	$1.6\times10^{-4}\pm7.9\times10^{-5}$	1.7×10^{-4}	2.0	−0.03	−0.07
$C_{5,2}$	$-3.7\times10^{-5}\pm8.1\times10^{-5}$	1.1×10^{-5}	0.5	−4.27	−0.60
$S_{5,2}$	$-2.7\times10^{-4}\pm7.4\times10^{-5}$	-3.4×10^{-4}	3.6	−0.20	0.91
$C_{5,3}$	$-2.2\times10^{-6}\pm8.2\times10^{-5}$	-8.3×10^{-6}	0.0	−0.74	0.08
$S_{5,3}$	$-9.5\times10^{-6}\pm7.5\times10^{-5}$	-4.1×10^{-5}	0.1	−0.77	0.42
$C_{5,4}$	$3.2\times10^{-4}\pm7.2\times10^{-5}$	3.0×10^{-4}	4.5	0.08	0.34
$S_{5,4}$	$5.0\times10^{-5}\pm8.2\times10^{-5}$	9.9×10^{-5}	0.6	−0.49	−0.59
$C_{5,5}$	$-2.3\times10^{-5}\pm8.7\times10^{-5}$	4.6×10^{-5}	0.3	−1.50	−0.79
$S_{5,5}$	$3.0\times10^{-4}\pm7.3\times10^{-5}$	2.2×10^{-4}	4.1	0.38	1.11
J_6	$1.37\times10^{-3}\pm8.2\times10^{-5}$	1.44×10^{-3}	16.7	−0.05	−0.87
J_7	$-7.9\times10^{-5}\pm1.2\times10^{-4}$	-8.8×10^{-5}	0.7	−0.11	0.08
J_8	$-6.8\times10^{-4}\pm1.1\times10^{-4}$	-7.0×10^{-4}	6.2	−0.03	0.17
J_9	$-3.5\times10^{-5}\pm1.0\times10^{-4}$	4.2×10^{-5}	0.3	−1.84	−0.75
J_{10}	$2.0\times10^{-4}\pm9.9\times10^{-5}$	2.6×10^{-4}	2.0	−0.22	−0.59

Note. All coefficients are estimated through degree 10, but we tabulate sectorial and tesseral coefficients only through degree 5 and zonal coefficients through degree 10. The corresponding coefficients derived from the shape model assuming a uniform density are also tabulated, along with the relative and statistical deviations of our estimate from the uniform density assumption. The reference radius for the expansion is 290 m, and the estimated $GM=4.8904\pm0.0009\ m^3/s^2$.

trajectory fit provides no information on area-to-mass ratio, but that of P58 has SNR~20 and, together with the absolute magnitude, indicates an equivalent diameter 1.9 cm.

Finally, we compute a joint estimate of the bounce location and time. Initially we computed this linearly using the empirical means and covariances of the Monte Carlo samples by solving the normal equations associated with them. This produced a believable estimate, but this method did not account for the non-Gaussian nature of P58. In order to produce a less biased estimate, we calculated the weighted mean and covariance of P58's samples, where the samples were weighted by their distance from P57's solution. We leveraged the fact that P57's Monte Carlo dispersions appeared Gaussian, which allowed us to use P57's empirical mean and covariance to weight P58's samples. This yielded the joint solution shown in Figure 15. We note that this joint solution falls on a bouldery area of Bennu's surface that is substantially devoid of fine material, which is consistent with the nature of a ricochet. A complete analysis of the bounce in light of the detailed topography of the area could isolate specific locations in the joint solution footprint that are consistent with the prebounce and postbounce trajectories.

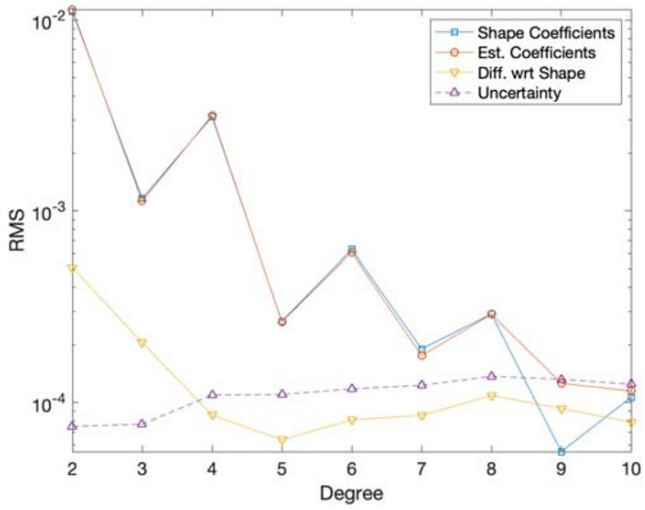

Figure 20. The RMS of gravitational spherical harmonic coefficients per degree. The uppermost curves depict the estimated gravity field and that obtained from the Bennu shape model assuming uniform density. The difference between these two fields is also depicted, as is the RMS of the coefficient uncertainties at each degree.

5.5. General Characteristics of Ejections and Impacts

We have so far identified several simultaneous ejection events and described a case where an ejection is linked directly to a concurrent impact. Now we turn to an examination of the properties of ejections and impacts in a broad sense. We limit the discussion here to those impacts and ejections having no more than 15° uncertainty in the latitude and longitude of the location. This limitation leaves 181 ejections and 166 impacts to be analyzed.

Figure 18 depicts the distribution of Bennu LST at the time and location of each ejection and impact. There is a clear enhancement of ejections during the afternoon and especially the evening on Bennu, even while there is a background of ejections taking place at all times of day. This is true both for the concentrated ejection events from Table 2 and the *sporadic* ejections that are so far not tied to an event. The LST for impacts appears more randomized, though there remains a slight enhancement of evening impacts. This may be a random fluctuation; however, suborbital trajectories that almost survive their first periapsis passage would tend to impact at an LST similar to that of their ejection, while others would be randomized. Thus, the slight enhancement in evening impacts could be related to that seen for ejections.

The afternoon/evening ejection enhancement is consistent with two hypotheses for ejection. Molaro et al. (2020) find that the diurnal thermal cycle has peak thermal stresses in the afternoon when maximum temperatures occur and then after nightfall due to rapid cooling. This leads them predict that ejections due to thermal fatigue would occur during this time. On the other hand, given Bennu's retrograde rotation, the afternoon and evening ejections arise from Bennu's forward-facing hemisphere, as defined by its heliocentric orbit. This is in line with predictions that meteoroid impacts will predominate on the leading hemisphere (Bottke et al., 2020). And yet our results do show a far more significant background of ejections on the morning hemisphere than is predicted by either model. We speculate that this is due to ejections caused by particle impacts, which has been demonstrated above for P57 and P58.

Figure 19 depicts the distribution of the sine of latitude for ejections and impacts, which should be uniform for an area-wise uniform distribution on a sphere. We separate the related ejection events from the sporadic (singleton) ejections in the plot in order to discern any significant differences between the two, though none is apparent. The 19 January event, with 14 associated ejections, dominates the distribution of events. Both ejections and impacts show an excess in the equatorial regions and are more sparse at the poles. For impacts, the equatorial excess is more pronounced and is not unexpected, given the fact that the equatorial region has the highest radius terrain, and so a decaying orbit is more likely to intersect with the surface in this region. For the ejections, we note that Bottke et al. (2020) predicts an excess of meteoroid impacts in the equatorial region, which is primarily a manifestation of lower projected areas onto the meteoroid impact plane in the polar regions. In contrast, Molaro et al. (2020) do not predict a deviation from uniform latitudinal distribution.

5.6. Gravity Estimate

We derived a particle-based gravitational field, truncated at degree and order 10, by simultaneously estimating the gravitational field for a number of well-observed particles. This served the dual purposes of constraining the gravitational field of Bennu for follow-on geophysical studies and facilitating more reliable orbit estimation for the many particles that did not have a solid gravitational signal, that is, those having few detections or short data arcs or both. The ongoing radio science investigation of the OSIRIS-REx spacecraft motion about Bennu will yield an independent estimate of Bennu's gravity field. These separate approaches, from spacecraft and particles, will be compared and unified in a forthcoming report, which will also consider the geophysics implications of Bennu's gravity field.

For this effort, we selected those particles with more than 30 detections and having observational arcs either more than 6 hr in length or covering more than 80% of the particle lifetime. The latter constraint allowed

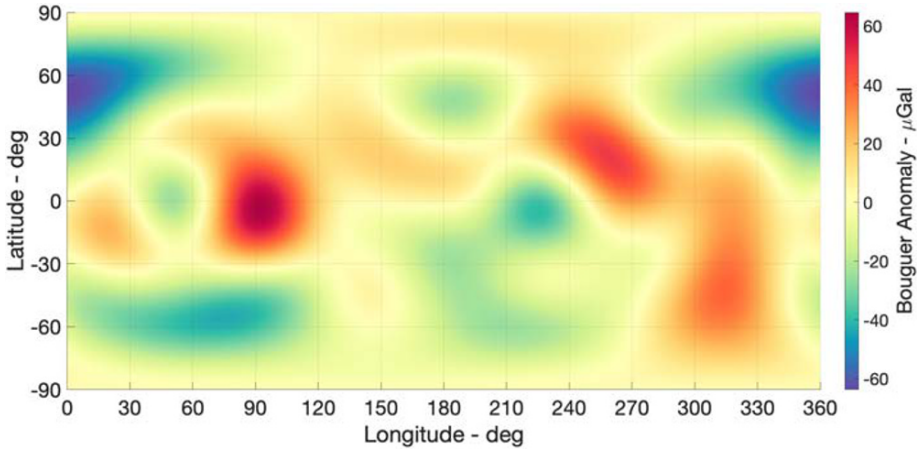

Figure 21. Bouguer anomaly map for Bennu's estimated gravity field. Red-orange (green-blue) regions indicate regions of higher (lower) surface accelerations than those derived from the shape assuming uniform density.

well-observed suborbital particles to be included in the gravity estimate. This led to a set of 20 particles, which are listed in Table 4, along with their relevant particulars such as arc length and number of detections.

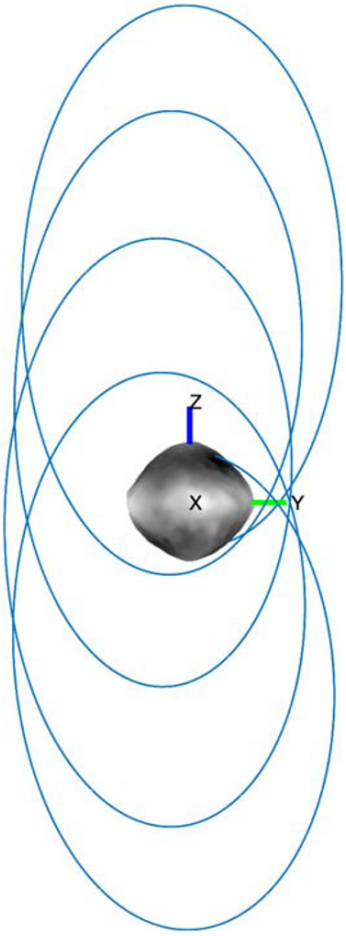

Figure 22. Trajectory of P1 as seen looking from the direction of the Sun.

The a priori values for the harmonic coefficients come directly from shape model integration, assuming constant density. We used the modified Kaula rule for Bennu to generate the a priori uncertainties (McMahon et al., 2018). Degree 1 terms, reflective of offsets between the center of mass and center of volume, were zeroed and not estimated. Based on higher-fidelity modeling from optical imaging, we enforced the assumption that Bennu is in simple rotation, and thus the $C_{2,1}$ and $S_{2,1}$ terms were zeroed and not estimated. When estimating the gravity field, we did estimate the rotation axis orientation, with a priori constraints from spacecraft radio science, but the particle tracking data are not strongly sensitive to spin axis orientation, and there was no appreciable deviation from the a priori values.

This 20-particle joint gravity estimate yielded Bennu's gravitational parameter, $GM = 4.8904 \pm 0.0009\ \mathrm{m}^3/\mathrm{s}^2$. This is consistent with the OSIRIS-REx postrendezvous estimate, which was $GM = 4.892 \pm 0.006\ \mathrm{m}^3\ \mathrm{s}^2$ (Scheeres et al., 2019). The spherical harmonic coefficients are listed in Table 5 with the full expansion through degree 5 and zonal terms through degree 10. The coefficients of the spherical harmonic expansion were well determined through degree 4, where all but two of the 19 coefficients through degree and order 4 have SNR>3. The full gravitational field with covariance is available from Chesley et al. (2019).

Figure 20 indicates the difference at each degree between our estimate and the shape-based (i.e., uniform density) field, along with the RMS uncertainty at each degree. From the plot it is clear that the particles are sensitive to gravitational harmonics through degree 8, though we are unable to distinguish nonuniform mass distribution beyond degree 3.

Figure 21 shows the map of the radial acceleration difference between the observed gravity field and the gravity computed from shape (uniform-density Bennu), which is often called the Bouguer anomaly map (Park et al., 2016). The Bouguer anomaly was mapped to the reference sphere (i.e., 290-m radius) for spherical harmonic coefficients up to degree 6,

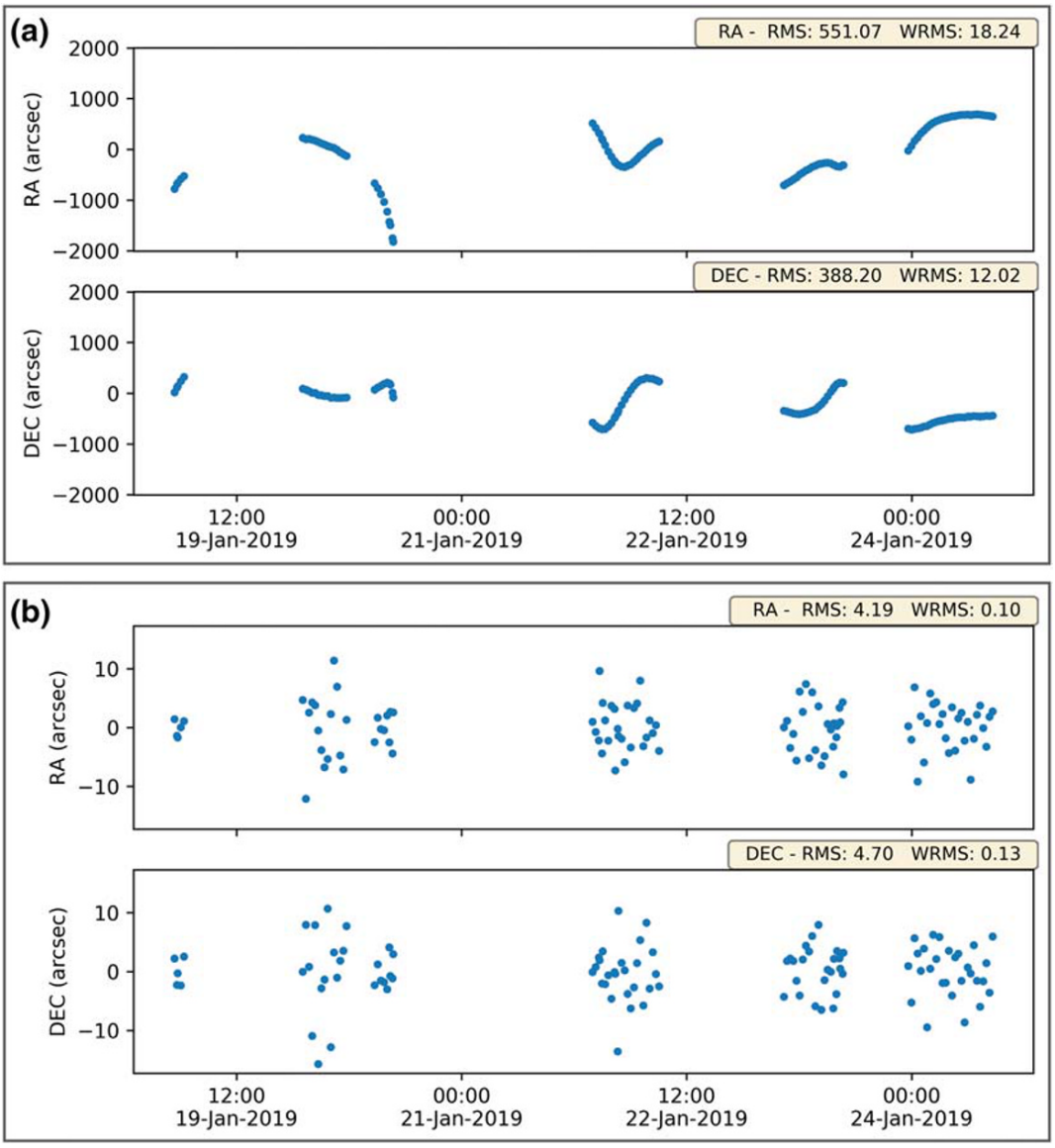

Figure 23. Postfit RA-DEC residuals for particle P1 when (a) neglecting the possibility of empirical accelerations and spacecraft position errors and (b) estimating these as a part of the fitting process.

excluding the degree 1 terms. The maximum Bouguer anomaly of ~65 μGal is at longitude 90° and near the equator.

5.7. Interpretation of Empirical Accelerations

In section 3, we described the details of the force model that we apply to the particles. As a part of the force modeling, we estimate any unmodeled forces that are required to keep the particle on its observed trajectory. These empirical forces are in many cases negligible, but in some cases not ignorable. To demonstrate the need for empirical forces, we consider as a case study the 1.7-cm particle P1. This particle follows a roughly polar orbit (Figure 22) with high apoapsis, mitigating some potential sources of force mismodeling, for example, gravity field, shadowing, and radiation from Bennu. Thus, while P1 is not an extraordinary case, it makes for a good example of behaviors commonly seen on particles with data arcs longer than about a half day.

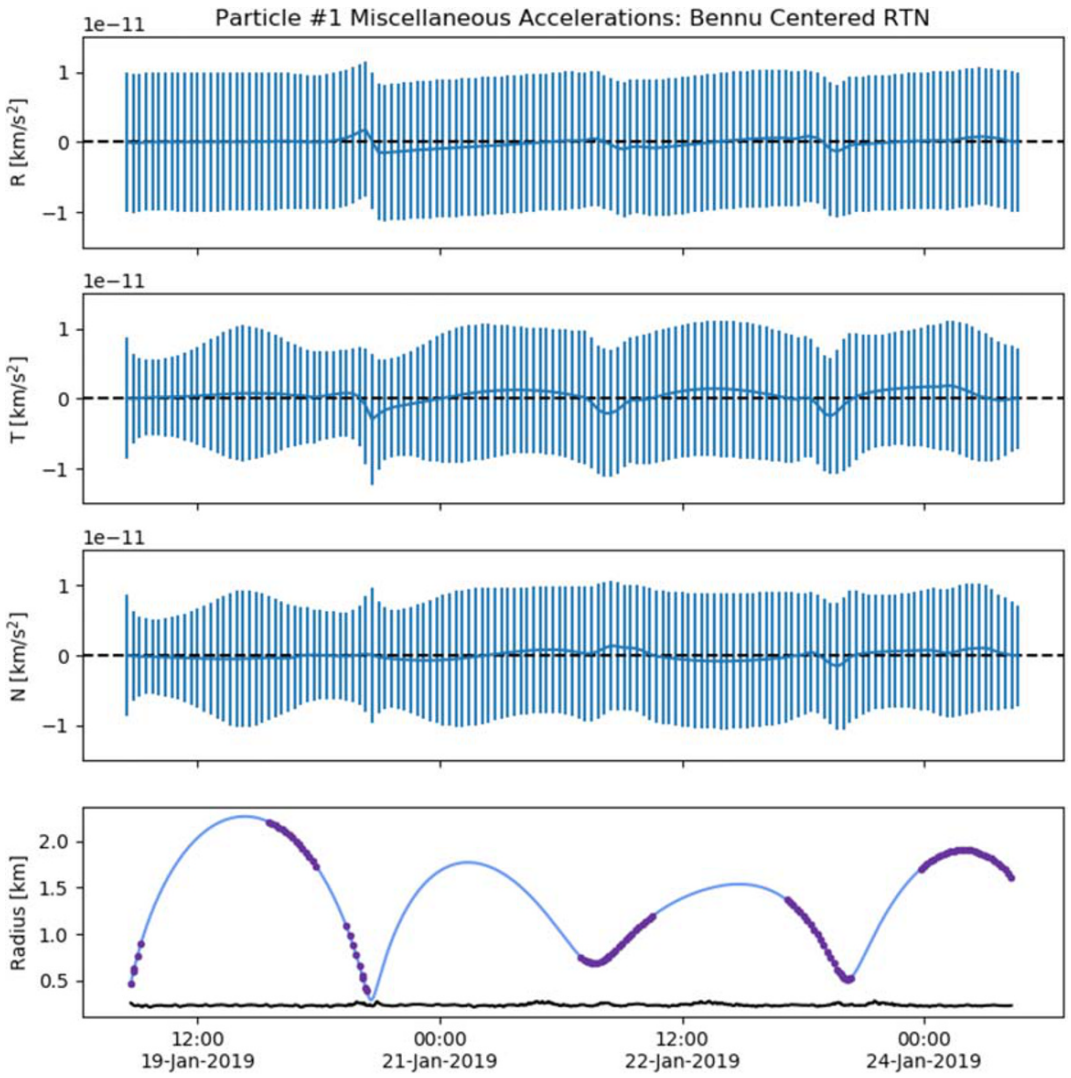

Figure 24. Empirical accelerations estimated for P1, projected into the Bennu-centered RTN frame. The bottom panel depicts the radii of the particle and subparticle terrain during the observation arc. Observation times are marked by dots in the bottom panel.

Despite the presumably simpler dynamical model that could be appropriate for P1, we could not obtain acceptable fits even with the full, detailed dynamical model including all of the known forces listed in Table 1. Figure 23a depicts the postfit RA-DEC residuals from such a fit, for which we find a collective WRMS of 15.0. Not only are the residuals large, but clear trends are visible, indicating dynamical mismodeling or systematic errors in observational modeling, rather than observational noise.

Next we ask whether spacecraft position errors could be the cause of the large residuals, and to this end, we estimate the spacecraft position error as described above in section 4.2, but still not allowing for empirical accelerations. While the resulting WRMS is much lower (~2.74), it is still poor, and more importantly, much of the signature seen in Figure 23a remains plainly apparent, though more muted. And even as the fit remains poor, the estimated corrections to the spacecraft trajectory are very large, as large as ±5 m, and even extending to 10 m briefly. This is an implausible deviation from the OSIRIS-REx spacecraft ephemeris estimate, which is expected to be within a few tens of centimeters. Thus, we conclude that spacecraft position errors alone cannot account for the poor residuals in Figure 23a.

Finally, we turn to estimating the empirical accelerations, while continuing to estimate the spacecraft position errors as before. As indicated in Figure 23b, the resulting postfit residuals are small (WRMS ~0.12) and

show no significant trends. At the same time, the estimated spacecraft position errors fell to realistic levels, with peaks in the range of 10 to 20 cm. The estimated empirical accelerations are plotted in Figure 24. In the figure, we observe that the estimated accelerations remain small, only a few times 10^{-12} km/s^2 and that the a priori constraint (10^{-11} km/s^2) tends to dominate the a posteriori uncertainty. The position deviations due to such an acceleration are roughly a few meters per day, consistent with the deviations in the residuals seen in Figure 23a. Although none of the individual elements of the empirical acceleration history are statistically significant, the ensemble effect is vital to obtaining a valid fit. There are surges in the empirical acceleration around the times of periapsis, which could be diagnostic of the source of the acceleration.

We are unable to point to a definitive explanation for these empirical accelerations, which anyway need not have a single source. Given that there appear to be surges in the acceleration near periapsis, and that other objects show a periodic signal matching the orbital period, there is the possibility that mismodeling of gravity or Bennu radiation (reflected visible light or thermal emission) are contributors. But we also see accelerations far from periapsis. The fact that some anomalous accelerations are present at higher altitudes points to other sources of mismodeling. Our assumption of Lambertian reflected radiation is certainly suspect, as discussed by Dellagiustina et al. (2019). Or a slowly varying effective area-to-mass ratio, due to a precessing spin orientation, could cause a modulation in the effective SRP. However, both of these possibilities would manifest most strongly in the Sun direction, which we do not see in Sun-centered RTN projections of the empirical accelerations. Despite the lack of clarity in the source of these accelerations, we do not so far see a compelling need to invoke mass loss, for example, through outgassing or fission, as a likely cause of these accelerations.

6. Summary and Conclusions

In this report we present a catalog of trajectories and related analyses for 313 particles seen in Bennu's environment. About two thirds of particles were on suborbital trajectories, one seventh departed on direct escape trajectories, and one fifth orbited Bennu for more than one complete revolution. We derived the sizes of the particles based on estimated area-to-mass ratios, combined with the photometric analyses presented by Hergenrother et al. (2020). The results reveal a population of flake-like particles with median axis ratio 0.27 and equivalent diameters ranging from 0.22–6.1 cm, with median 0.74 cm.

The present results are not final as there are still more data to be processed, and future mission phases may yield new particle detections. Furthermore, even among the current data we will be revisiting failed and discarded solutions to obtain the correct solution whenever possible. Monte Carlo analysis of all impacts and ejections may yield additional cases of ejection caused by particle impacts, as well as new and expanded sets of particles associated by concurrent ejection events. Additional links likely remain to be found, and several apparently related particles have yet to be definitively connected.

Selection effects are sure to have affected the particle catalog that we have developed. Fast-moving particles leave the scene too rapidly to allow a suitable data set to be collected. Similarly, very slow ejections are aloft too short of a time to afford a sufficient number of detections. And small particles are below the detection threshold of the camera. Thus, our catalog is predominantly composed of particles that are large enough ($\gtrsim$ 2 mm) and remain within a few kilometers of Bennu for at least a few hours. Additionally, the imaging cadence for particle detections has been highly variable across the various OSIRIS-REx mission phases, which raises challenges in discerning if the level of Bennu activity depends on heliocentric distance. Future work may allow better insight into the debiased particle population and activity levels.

We identified several ejection events with multiple simultaneous ejections emerging from the same location. While some of these events have been previously reported, others are new, and we made no use of external information in identifying the particles associated with the links. Given that we did not make presumptions or enforce constraints on the ejection circumstances for the individual particle fits, the fact that we found 10 events comprising 40 particles altogether is a reassuring argument that our trajectories are generally reliable.

We also identified a case where a particle ricocheted from the surface, demonstrating that not all ejections are related to surface processes. The postbounce orbit is at substantially lower inclination and eccentricity, which should be typical of other similar events, suggesting that bouncing particles are likely to eventually reimpact in the equatorial region. This may provide a pathway to understanding the overall role of particle ejections

and associated mass movement on Bennu's surface, which likely has a connection to the global shaping process pointed to by Scheeres et al. (2019) in relation to the Roche lobe of Bennu. This discovery also allowed us to compute a coefficient of restitution, which has implications for the mechanical properties of the boulders on Bennu's surface, as well as that of the particles.

Taking a subset of well-observed particles, we derived a Bennu gravity field composed of spherical harmonics having clear signal through degree 8 and revealing density inhomogeneities through degree 3. We await companion results from spacecraft tracking, which will serve as a vital validation of these results, and which can be combined to yield a definitive gravity field.

Despite striving for a complete and high-fidelity force model for our particle trajectory propagation, we found it necessary to apply estimated empirical forces in order to allow the computed particles trajectories to follow the observed paths. These empirical accelerations often have a periodic signal matching the orbit period, suggesting mismodeling of one or more Bennu-related forces, for example, emitted or reflected radiation from Bennu onto the particle. We consider gravity mismodeling as an unlikely explanation because even for an individual particle fit where the gravity was allowed to correct the inconsistencies, the postfit residuals could not be reduced to acceptable levels. Particles that repeatedly entered Bennu's shadow appear to show a stronger orbit periodic signal, at least in a few cases, pointing to the possibility that our eclipse model is somehow deficient. And there remains the possibility that non-Lambertian scattering and shape-specific effects on reflected radiation pressure are important.

Thus, while including these accelerations is vital to fit quality and trajectory accuracy, we cannot point to a definitive source of the acceleration. Though mass loss due to fission or outgassing cannot be ruled out, there is no compelling argument that these processes must be acting on the particles. More intriguing in this regard are the several apparently related particles that are following extraordinarily similar orbits, even approaching to within a few meters at relative velocities <1 mm/s, but for which a linked trajectory solution is elusive. This is in stark contrast to the ease with which most linked orbits fall into place. This could be a manifestation of an impulsive trajectory correction, as would be expected for the fission of a small grain from a larger and rapidly spinning particle. A more complete understanding of these cases is left as future work.

The results reported here have implications for the underlying cause of the ejections. Our findings generally agree with the predictions of Molaro et al. (2020) regarding fatigue fracturing due to the diurnal thermal cycle, in particular in regard to the size distribution of the fractured particles, assuming our distribution of particle axis ratios. The prevalence of ejections in the evening and afternoon is also in accord, though our reduced number of ejections at polar latitudes does not match the thermal fracturing models. On the other hand, the meteoroid impact hypothesis proposed by Bottke et al. (2020) makes predictions that are also consistent with our results. In particular, they predict most ejections will be on the afternoon/evening hemisphere, with an enhancement in the equatorial regions, which agrees well with our findings. The observation of over a hundred particles being simultaneously released in ejection events (Lauretta et al., 2019) seems to point more toward the meteoroid hypothesis, though catastrophic releases of internal thermal stresses are known to occur in terrestrial settings. Neither of these hypotheses predict the significant number of ejections seen from the opposite (morning) hemisphere, which could be a manifestation of ejections spawned by low-velocity particle impacts, either through ricocheting or lofting of different particles.

There is certainly no reason to insist that a single mechanism drives the particle ejection phenomenon. The notion that thermal fracturing is grinding the surface into particles that can later be lofted by meteoroid bombardment is one way that these mechanisms can be working in concert. This idea is particularly attractive given that our particle sizes are an excellent match to those for thermal fracturing, while the latitudinal distribution of ejections is a better match to the meteoroid impact prediction. When combined with a background of ejections that are spawned by particle impacts, we have a cohesive story that meets our observational constraints. There may also be a superposition of thermally driven ejections in addition to those arising from meteoroid impacts. Indeed, the mass loss mechanism seen on Phaethon at its perihelion (Li & Jewitt, 2013) could be taking place at Bennu, though at a dramatically reduced rate due to the higher heliocentric distance. Comparison of more refined ejection location information with high-resolution imagery may shed further light on this question.

An important question is how prevalent the particle ejection phenomenon is across the near-Earth asteroid population, and even in the main asteroid belt. Given the report from Granvik et al. (2016) that only the small and dark asteroids are being catastrophically disrupted at small heliocentric distances, the question looms large as to whether the phenomenon represented by Bennu's particles is primarily associated with C-complex asteroids. At Bennu, the particles were discovered with an extraordinarily wide field-of-view instrument operated in a novel way so that the primary target was heavily overexposed. This type of instrumentation and mode of operation has not been deployed in previous asteroid missions, but the discovery of particles around Bennu may motivate similar observations at other asteroids in the future.

Appendix A: Average Cross Section of a Tumbling Spheroid

We consider a tumbling ellipsoid with semiaxes a, a, and b, defined by the equation

$$x^2/a^2 + y^2/a^2 + z^2/b^2 = 1.$$

In the body-fixed frame, we indicate the direction from the center of the ellipsoid to the Sun as $\hat{\mathbf{u}} = (\cos\alpha\cos\delta,\ \sin\alpha\cos\delta,\ \sin\delta)$. The cross section of the ellipsoid visible from the Sun is given by the projection of the ellipsoid on the plane normal to $\hat{\mathbf{u}}$, which is defined by the directions $\hat{\mathbf{v}} = (-\sin\alpha,\ \cos\alpha,\ 0)$ and $\hat{\mathbf{w}} = (-\cos\alpha\sin\delta,\ -\sin\alpha\sin\delta,\ \cos\delta)$. Given the corresponding coordinate system (u,w), the projected ellipse is

$$u^2/a^2 + w^2/(a^2\sin^2\delta + b^2\cos^2\delta) = 1$$

and therefore the area of the cross section is $A = \pi a\sqrt{a^2\sin^2\delta + b^2\cos^2\delta}$.

We assume that, because of the tumbling rotation state, the body-fixed z axis is uniformly distributed in space over time. This assumption is equivalent to having a uniform distribution of $\hat{\mathbf{u}}$ in the body-fixed frame. Therefore, the average cross-section can be computed as

$$\bar{A} = \frac{1}{2}\int_{-1}^{1} A\ d(\sin\delta) = \frac{\pi a^2}{2}\int_{-1}^{1}\sqrt{\sin^2\delta + p^2\cos^2\delta}\ d(\sin\delta) = \pi a^2 f(p),$$

where $p = b/a$. The definite integral can be evaluated to obtain

$$f(p) = \begin{cases} \dfrac{\sqrt{1-p^2} + p^2\,\mathrm{arcsinh}(\sqrt{1-p^2}/p)}{2\sqrt{1-p^2}} & p<1 \\ 1 & p = 1\,. \\ \dfrac{\sqrt{p^2-1} + p^2\arcsin(\sqrt{p^2-1}/p)}{2\sqrt{p^2-1}} & p > 1 \end{cases}$$

Acknowledgments

This material is based upon work supported by NASA under Contract NNM10AA11C issued through the New Frontiers Program. This research was conducted in part at the Jet Propulsion Laboratory, California Institute of Technology, under a contract with the National Aeronautics and Space Administration. B. R. acknowledges funding support from the Royal Astronomical Society (RAS) and the U.K. Science and Technologies Facilities Council (STFC). The work of D.V. was partially funded by the Czech Science Foundation (Grant 18-06083S). Special thanks to B. Semenov and the Navigation and Ancillary Information Facility (NAIF) team at JPL, who provided crucial support in our effort to fit the particle detections and analyze the associated results. We are grateful to H. Roper for her assistance in preparing the figures, and we thank M. Daly and M. Al Asad for sharing the off-Bennu OLA detections. Finally, we thank the entire OSIRIS-REx Team for making the encounter with Bennu possible.

Data Availability Statement

NavCam 1 images are or will be available via the TAGCAMS bundle in the Planetary Data System (https://sbn.psi.edu/pds/resource/orex/tagcams.html) (Bos et al., 2019). Observational and derived data used in this work are available from Chesley et al. (2019). Our orbit estimation software is derived from MIRAGE, now called MONTE, which is available by license from https://montepy.jpl.nasa.gov website. Our trajectory estimation relies on classical orbit determination algorithms as previously implemented by Brozović and Jacobson (2017). We also made use of the SPICE software suite using kernels publicly available on the NAIF website (https://naif.jpl.nasa.gov/naif/index.html). The reduction and processing of angular position measurements is covered by Murray (1983), the propagation of trajectories and treatment of time is described by, among others Moyer (2003), and the estimation approach that we use is that of Bierman (1977). All parameters needed to reproduce our results are described in the text. The raw numbers for all figures in the text area can be obtained from Chesley et al. (2019). ©2019.

References

Barnouin, O. S., Daly, M. G., Palmer, E. E., Gaskell, R. W., Weirich, J. R., Johnson, C. L., et al. (2019). Shape of (101955) Bennu indicative of a rubble pile with internal stiffness. *Nature Geoscience*, *12*(4), 247–252. https://doi.org/10.1038/s41561-019-0330-x

Bierman, G. J. (1977). *Factorization methods for discrete sequential estimation*: Academic Press.
Borderies, N., & Longaretti, P.-Y. (1990). A new treatment of the albedo radiation pressure in the case of a uniform albedo and of a spherical satellite. *Celestial Mechanics and Dynamical Astronomy*, *49*(1), 69–98. https://doi.org/10.1007/BF00048582
Bos, B., Jackman, C., & Lauretta, D. S. (2019). Origins, Spectral Interpretation, Resource Identification, Security, Regolith Explorer (OSIRIS-REx): Touch-and-Go Camera Suite (TAGCAMS) bundle, urn:nasa:pds:orex.tagcams.
Bos, B. J., Nelson, D. S., Pelgrift, J. Y., Liounis, A. J., Doelling, D., Norman, C. D., et al. (2020). In-flight calibration and performance of the OSIRIS-REx Touch And Go Camera System (TAGCAMS). *Space Science Reviews*, *216*, 71. https://doi.org/10.1007/s11214-020-00682-x
Bos, B. J., Ravine, M. A., Caplinger, M., Schaffner, J. A., Ladewig, J. V., Olds, R. D., et al. (2018). Touch And Go Camera System (TAGC AMS) for the OSIRIS-REx asteroid sample return mission. *Space Science Reviews*, *214*(1), 37. https://doi.org/10.1007/s11214-017-0465-2
Bottke, W. F., Moorhead, A., Connolly, H. C., Hergenrother, C. W., Molaro, J. L., Michel, P., et al. (2020). Meteoroid impacts as a source of Bennu's particle ejection events. *Journal of Geophysical Research: Planets*, *125*, e2019JE006282. https://doi.org/10.1029/2019JE006282
Bottke, J., Vokrouhlický, D., Rubincam, D. P., & Nesvorný, D. (2006). The Yarkovsky and Yorp effects: Implications for asteroid dynamics. *Annual Review of Earth and Planetary Sciences*, *34*, 157–191. https://doi.org/10.1146/annurev.earth.34.031405.125154
Brozović, M., & Jacobson, R. A. (2017). The orbits of Jupiter's irregular satellites. *The Astronomical Journal*, *153*(4), 147. https://doi.org/10.3847/1538-3881/aa5e4d
Capaccioni, F., Cerroni, P., Coradini, M., Farinella, P., Flamini, E., Martelli, G., et al. (1984). Shapes of asteroids compared with fragments from hypervelocity impact experiments. *Nature*, *308*(5962), 832–834. https://doi.org/10.1038/308832a0
Chesley, S., Hergenrother, C., Adam, C. D., Alkiek, K., Balram-Knutson, S., Becker, K., et al. (2019). Supplementary data for Bennu particle analysis. https://doi.org/10.6084/m9.figshare.11328398
Clark, B. E., Binzel, R. P., Howell, E. S., Cloutis, E. A., Ockert-Bell, M., Christensen, P., et al. (2011). Asteroid (101955) 1999 RQ36: Spectroscopy from 0.4 to 2.4 μm and meteorite analogs. *Icarus*, *216*(2), 462–475. https://doi.org/10.1016/j.icarus.2011.08.021
Collins, B. D., Stock, G. M., Eppes, M.-C., Lewis, S. W., Corbett, S. C., & Smith, J. B.(2018). Thermal influences on spontaneous rock dome exfoliation. *Nature Communications*, *9*, 762. https://doi.org/10.1038/s41467-017-02728-1
Daly, M. G., Barnouin, O. S., Dickinson, C., Seabrook, J., Johnson, C. L., Cunningham, G., et al. (2017). The OSIRIS-REx Laser Altimeter (OLA) investigation and instrument. *Space Science Reviews*, *212*(1–2), 899–924. https://doi.org/10.1007/s11214-017-0375-3
Dankowicz, H. (1994). Some special orbits in the two-body problem with radiation pressure. *Celestial Mechanics and Dynamical Astronomy*, *58*, 353–370. https://doi.org/10.1007/BF00692010
Dankowicz, H. (1995). The two-body problem with radiation pressure in a rotating reference frame. *Celestial Mechanics and Dynamical Astronomy*, *61*, 287–313. https://doi.org/10.1007/BF00051898
Delbo, M., Libourel, G., Wilkerson, J., Murdoch, N., Michel, P., Ramesh, K. T., et al. (2014). Thermal fatigue as the origin of regolith on small asteroids. *Nature*, *508*(7495), 233–236. https://doi.org/10.1038/nature13153
Dellagiustina, D. N., Emery, J. P., Golish, D. R., Rozitis, B., Bennett, C. A., Burke, K. N., et al. (2019). Properties of rubble-pile asteroid (101955) Bennu from OSIRIS-REx imaging and thermal analysis. *Nature Astronomy*, *3*, 341–351. https://doi.org/10.1038/s41550-019-0731-1
Denneau, L., Jedicke, R., Grav, T., Granvik, M., Kubica, J., Milani, A., et al. (2013). The Pan-STARRS moving object processing system. *Publications of the Astronomical Society of the Pacific*, *125*(926), 357. https://doi.org/10.1086/670337
Fröhlich, C., & London, J. (1986). Revised instruction manual on radiation instruments and measurements(*WMO/TD-No. 149*): World Climate Research Programme, WMO/ICSU Joint Scientific Committee.
Granvik, M., Morbidelli, A., Jedicke, R., Bolin, B., Bottke, W. F., Beshore, E., et al. (2016). Super-catastrophic disruption of asteroids at small perihelion distances. *Nature*, *530*(7590), 303–306. https://doi.org/10.1038/nature16934
Hamilton, V. E., Simon, A. A., Christensen, P. R., Reuter, D. C., Clark, B. E., Barucci, M. A., et al. (2019). Evidence for widespread hydrated minerals on asteroid (101955) Bennu. *Nature Astronomy*, *3*, 332–340. https://doi.org/10.1038/s41550-019-0722-2
Hergenrother, C. W., Maleszewski, C., Li, J.-Y., Pajola, M., Chesley, S. R., French, A. S., et al. (2020). Photometry of particles ejected from active asteroid (101955) Bennu. *Journal of Geophysical Research: Planets*, *125*, e2020JE006381. https://doi.org/10.1029/2020JE006381
Hergenrother, C. W., Maleszewski, C. K., Nolan, M. C., Li, J. Y., Drouet D'Aubigny, C. Y., Shelly, F. C., et al. (2019). The operational environment and rotational acceleration of asteroid (101955) Bennu from OSIRIS-REx observations. *Nature Communications*, *10*, 1291. https://doi.org/10.1038/s41467-019-09213-x
Hsieh, H. H., & Jewitt, D. (2006). A population of comets in the main asteroid belt. *Science*, *312*(5773), 561–563. https://doi.org/10.1126/science.1125150
Jekeli, C. (1983). A numerical study of the divergence of spherical harmonic series of the gravity and height anomalies at the earth's surface. *Bulletin Géodésique*, *57*(1), 10–28. https://doi.org/10.1007/BF02520909
Jewitt, D., Agarwal, J., Weaver, H., Mutchler, M., & Larson, S. (2013). The extraordinary multi-tailed main-belt Comet P/2013 P5. *The Astrophysical Journal Letter*, *778*(1), L21. https://doi.org/10.1088/2041-8205/778/1/L21
Jewitt, D., Hsieh, H., & Agarwal, J. (2015). The active asteroids. In P. Michel, F. DeMeo, & W. F. Bottke (Eds.), *Asteroids IV* (pp. 509–531). Tucson: University Arizona Press
Lauretta, D. S., Hergenrother, C. W., Chesley, S. R., Leonard, J. M., Pelgrift, J. Y., Adam, C. D., et al. (2019). Episodes of particle ejection from the surface of the active asteroid (101955) Bennu. *Science*, *366*(6470). https://doi.org/10.1126/science.aay3544
Leonard, J. M., Adam, C. D., Pelgrift, J. Y., Lessac-Chenen, E. J., Nelson, D. S., Antreasian, P. G., et al. (2020). Initial orbit determination and event reconstruction from estimation of particle trajectories about (101955) Bennu. *Earth and Space Science*, *7*, e2019EA000937. https://doi.org/10.1029/2019EA000937
Li, J., & Jewitt, D. (2013). Recurrent perihelion activity in (3200) Phaethon. *The Astronomical Journal*, *145*(6), 154. https://doi.org/10.1088/0004-6256/145/6/154
Liounis, A. J., Small, J. L., Swenson, J. C., Lyzhoft, J. R., Ashman, B. W., Getzandanner, K. M., et al. (2020). Autonomous detection of particles and tracks in optical images. *Earth and Space Science*, *7*, e2019EA000843. https://doi.org/10.1029/2019EA000843
McMahon, J. W., Scheeres, D. J., Chesley, S. R., French, A., Brack, D., Farnocchia, D., et al. (2020). Dynamical evolution of simulated particles ejected from Asteroid Bennu. *Journal of Geophysical Research: Planets*, *125*, e2019JE006229. https://doi.org/10.1029/2019JE006229
McMahon, J. W., Scheeres, D. J., Hesar, S. G., Farnocchia, D., Chesley, S., & Lauretta, D. (2018). The OSIRIS-REx radio science experiment at Bennu. *Space Science Reviews*, *214*(1), 43. https://doi.org/10.1007/s11214-018-0480-y
Michikami, T., Hagermann, A., Kadokawa, T., Yoshida, A., Shimada, A., Hasegawa, S., & Tsuchiyama, A. (2016). Fragment shapes in impact experiments ranging from cratering to catastrophic disruption. *Icarus*, *264*, 316–330. https://doi.org/10.1016/j.icarus.2015.09.038

Mignard, F., & Henon, M. (1984). About an unsuspected integrable problem. *Celestial Mechanics*, *33*(3), 239–250.
Milani, A., La Spina, A., Sansaturio, M. E., & Chesley, S. R. (2000). The asteroid identification problem. III. Proposing identifications. *Icarus*, *144*(1), 39–53. https://doi.org/10.1006/icar.1999.6261
Milani, A., Sansaturio, M. E., & Chesley, S. R. (2001). The asteroid identification problem IV: Attributions. *Icarus*, *151*(2), 150–159. https://doi.org/10.1006/icar.2001.6594
Molaro, J. L., Hergenrother, C. W., Chesley, S. R., Walsh, K. J., Hanna, R. D., Haberle, C. W., et al. (2020). Thermal fatigue as a driving mechanism for activity on asteroid Bennu. *Journal of Geophysical Research: Planets*, *125*, e2019JE006325. https://doi.org/10.1029/2019JE006325
Moyer, T. D. (2003). *Formulation for observed and computed values of deep space network data types for navigation*: Wiley.
Murray, C. A. (1983). *Vectorial astrometry*: CRC Press.
Park, R. S., Konopliv, A. S., Bills, B. G., Rambaux, N., Castillo-Rogez, J. C., Raymond, C. A., et al. (2016). A partially differentiated interior for (1) Ceres deduced from its gravity field and shape. *Nature*, *537*(7621), 515–517. https://doi.org/10.1038/nature18955
Pelgrift, J. Y., Lessac-Chenen, E. J., Adam, C. D., Leonard, J. M., Nelson, D. S., McCarthy, L., et al. (2019). Reconstruction of Bennu particle events from sparse data. *Earth and Space Science*, *7*, e2019EA000938. https://doi.org/10.1029/2019EA000938
Reimond, S., & Baur, O. (2016). Spheroidal and ellipsoidal harmonic expansions of the gravitational potential of small Solar System bodies. Case study: Comet 67P/Churyumov-Gerasimenko. *Journal of Geophysical Research: Planets*, *121*, 497–515. https://doi.org/10.1002/2015JE004965
Richter, K., & Keller, H. U. (1995). On the stability of dust particle orbits around cometary nuclei. *Icarus*, *114*(2), 355–371.
Rieger, S. M., Scheeres, D. J., & Barbee, B. (2019). Orbital stability regions for hypothetical natural satellites of (101955) Bennu. *Journal of Spacecraft and Rockets*, *56*(3), 789–800. https://doi.org/10.2514/1.A34160
Rosengren, A. J., & Scheeres, D. J. (2014). On the Milankovitch orbital elements for perturbed Keplerian motion. *Celestial Mechanics and Dynamical Astronomy*, *118*(3), 197–220. https://doi.org/10.1007/s10569-013-9530-7
Rozitis, B., Emery, J. P., Siegler, M. A., Susorney, H. C. M., Molaro, J. L., Hergenrother, C. W., & Lauretta, D. S. (2020). Implications for ice stability and particle ejection from high-resolution temperature modeling of asteroid (101955) Bennu. *Journal of Geophysical Research: Planets*, *125*, e2019JE006323. https://doi.org/10.1029/2019JE006323
Rozitis, B., & Green, S. F. (2011). Directional characteristics of thermal-infrared beaming from atmosphereless planetary surfaces—A new thermophysical model. *Monthly Notices of the Royal Astronomical Society*, *415*(3), 2042–2062. https://doi.org/10.1111/j.1365-2966.2011.18718.x
Rozitis, B., & Green, S. F. (2012). The influence of rough surface thermal-infrared beaming on the Yarkovsky and YORP effects. *Monthly Notices of the Royal Astronomical Society*, *423*(1), 367–388. https://doi.org/10.1111/j.1365-2966.2012.20882.x
Rozitis, B., & Green, S. F. (2013). The influence of global self-heating on the Yarkovsky and YORP effects. *Monthly Notices of the Royal Astronomical Society*, *433*(1), 603–621. https://doi.org/10.1093/mnras/stt750
Sánchez, P., & Scheeres, D. J. (2014). The strength of regolith and rubble pile asteroids. *Meteoritics and Planetary Science*, *49*(5), 788–811. https://doi.org/10.1111/maps.12293
Scheeres, D. J. (1999). Satellite dynamics about small bodies: Averaged solar radiation pressure effects. *The Journal of the Astronautical Sciences*, *47*, 25–46.
Scheeres, D. J. (2012a). Orbit mechanics about asteroids and comets. *Journal of Guidance, Control and Dynamics*, *35*(3), 987–997.
Scheeres, D. J. (2012b). *Orbital motion in strongly perturbed environments: Applications to asteroid, comet and planetary satellite orbiters*. Springer-Praxis, London (UK).
Scheeres, D. J., Britt, D., Carry, B., & Holsapple, K. A. (2015). Asteroid interiors and morphology, *Asteroids IV* (pp. 745–766). https://doi.org/10.2458/azu_uapress_9780816532131-ch038
Scheeres, D. J., & Marzari, F. (2002). Spacecraft dynamics far from a comet. *The Journal of the Astronautical Sciences*, *50*(1), 35–52.
Scheeres, D. J., McMahon, J. W., French, A. S., Brack, D. N., Chesley, S. R., Farnocchia, D., et al. (2019). The dynamic geophysical environment of (101955) Bennu based on OSIRIS-REx measurements. *Nature Astronomy*, *3*, 352–361. https://doi.org/10.1038/s41550-019-0721-3
Tapley, B. D., Schutz, B. E., & Born, G. H. (2004). *Statistical orbit determination*. Burlington: Academic Press. https://doi.org/10.1016/B978-012683630-1/50025-4
Vokrouhlický, D. (1998). Diurnal Yarkovsky effect as a source of mobility of meter-sized asteroidal fragments. I. Linear theory. *Astronomy and Astrophysics*, *335*, 1093–1100.
Vokrouhlický, D., Bottke, W. F., Chesley, S. R., Scheeres, D. J., & Statler, T. S. (2015). The Yarkovsky and YORP effects. In P. Michel, F. DeMeo, & W. F. Bottke (Eds.), *Asteroids IV* (pp. 509–531). Tucson: Univ. Arizona Press.
Werner, R. A. (1997). Spherical harmonic coefficients for the potential of a constant-density polyhedron. *Computers and Geosciences*, *23*(10), 1071–1077. https://doi.org/10.1016/S0098-3004(97)00110-6
Werner, R. A., & Scheeres, D. J. (1996). Exterior gravitation of a polyhedron derived and compared with harmonic and mascon gravitation representations of asteroid 4769 Castalia. *Celestial Mechanics and Dynamical Astronomy*, *65*(3), 313–344. https://doi.org/10.1007/BF00053511